

**Simulating and Controlling the Performance of  $\text{Si}_3\text{N}_4$   
Micro-mechanical Resonators for Cavity Optomechanics**

by

**Gabriel G. T. Assumpção**

A thesis submitted to the  
Faculty of the Honors Program of the  
University of Colorado Boulder in partial fulfillment  
for a Latin honors designation with the degree of  
Bachelors of Arts, Physics  
Department of Physics

2017

This thesis entitled:  
Simulating and Controlling the Performance of  $\text{Si}_3\text{N}_4$  Micro-mechanical Resonators for Cavity  
Optomechanics  
written by Gabriel G. T. Assumpção  
has been approved for the Department of Physics

---

Prof. Cindy Regal  
Thesis Advisor, Department of Physics

---

Prof. John Cumalat  
Honors Council Representative, Department of Physics

---

Dr. Divya Vernerey  
Department of Mathematics

---

Prof. Konrad Lehnert  
Department of Physics

Date \_\_\_\_\_

The final copy of this thesis has been examined by the signatories, and we find that both the content and the form meet acceptable presentation standards of scholarly work in the above mentioned discipline.

Assumpção, Gabriel G. T. (B.A., Physics)

Simulating and Controlling the Performance of  $\text{Si}_3\text{N}_4$  Micro-mechanical Resonators for Cavity  
Optomechanics

Thesis directed by Prof. Cindy Regal

Thesis Advisor, Department of Physics

In the new field of Cavity Optomechanics the modes of a mechanical oscillator are strongly coupled to the resonant modes of a cavity, which enables the use of optical techniques, such as laser cooling, to manipulate and study oscillators. Oscillators with small mechanical dissipation, when interacting with low-loss, intense cavity field, can be cooled down to their harmonic ground state, a true breakthrough allowing for the study of the intrinsic quantum behavior of macroscopic objects. It is of interest, therefore, to use and develop mechanical oscillators with very small loss, or, in other words, very small coupling with the thermal bath and environment. One of the best materials in this sense,  $\text{Si}_3\text{N}_4$ , has been used in many optomechanical experiments due to their large quality factors, low optical absorption, and high mode frequencies. Nonetheless, modifications of membrane  $\text{Si}_3\text{N}_4$  such as trampolines and phononic crystals (PnC) have shown significant improvement of in their quality factor. This thesis describes new  $\text{Si}_3\text{N}_4$  resonator designs, the flower and the web, that uses both the trampoline and PnC characteristics in order to provide even higher quality factors and frequencies. By enabling better resonators, the new designs are also very suitable in extreme force sensing applications. Moreover, besides discussing how to attenuate mechanical losses, this thesis also contains heating models for  $\text{Si}_3\text{N}_4$ , which corroborate the extremely low optical absorption essential to the most ambitious cavity optomechanics experiments.

## **Dedication**

A Eliane e Altair, por uma existência livre de penúrias e repleta de apoio e carinho.

## Acknowledgements

My participation in the engaging research being done by the Regal group has been greatly helped by a striking group of benefactors. Many of the good ideas presented in this thesis were originally thought by Ran, for which I'm deeply grateful. At times it seemed that my function was, most of the time, to adapt Ran's ideas to working COMSOL models (no small feat on itself), but Ran also gave me great freedom to explore and patiently play around with the models, from which emerged the web and flower designs.

Ran and Tom also kept bringing me back to focus when I got caught up in some technicality or trivial pursuit, for which I'm also very grateful. In particular, the conversations where I could put everything in perspective and clarify my thinking were exceedingly helpful.

I also thank Bob for the reassuring assistance in the early projects that are not part of this thesis. I used to wonder how I could be useful if I barely new any physics, but Bob guided me through projects that taught me a great deal.

Nir was very patient not only in helping me understand the data to be used with the thermal models, but also in encouraging me to be more proactive, remembering that "slow is fast."

Finally, I'm very grateful for the entire array of help, encouragement, and guidance from Cindy. From giving the opportunity to work in the lab and get involved with a truly exciting field, to giving me advice on future career paths, and providing useful feedback on my performance in between, I can't imagine a better learning experience and introduction to an entire professional field.

## Contents

| <b>Chapter</b> |   |
|----------------|---|
| <b>1</b>       | <b>Introduction</b> <span style="float: right;"><b>1</b></span>                         |
| 1.1            | Context . . . . . 1   |
| 1.2            | Outline . . . . . 5   |
| <b>2</b>       | <b>Cavity optomechanics</b> <span style="float: right;"><b>7</b></span>                 |
| 2.1            | Basic Theory of Cavity Optomechanics . . . . . 7  |
| 2.2            | Membrane-in-the-middle Systems . . . . . 13   |
| 2.3            | Silicon Nitride Membrane Experiments . . . . . 14                                       |
| 2.3.1          | Observation of Quantum Behavior . . . . . 14  |
| 2.3.2          | Conversion Between Optical and Microwave Signals . . . . . 15                           |
| 2.3.3          | Magnetic Resonance Force Detection using SiN Membranes . . . . . 18                     |
| <b>3</b>       | <b>Loss mechanisms for Silicon Nitride</b> <span style="float: right;"><b>22</b></span> |
| 3.1            | Introduction . . . . . 22   |
| 3.1.1          | Internal Losses . . . . . 23  |
| 3.1.2          | External Losses . . . . . 26  |
| 3.2            | Loss-Attenuating Designs . . . . . 27   |
| 3.2.1          | Silicon Substrate PnC: Theory and Experiment . . . . . 28                               |
| 3.2.2          | An Overview of Trampolines . . . . . 36   |
| 3.2.3          | Silicon Nitride PnC with Membrane-like Defect . . . . . 37                              |

|          |   |           |
|----------|---|-----------|
| <b>4</b> | <b>FEM modeling of Hybrid Trampoline-PnC Designs</b>                      | <b>40</b> |
| 4.1      | Introduction . . . . .  | 40        |
| 4.2      | External Loss Simulation via Perfectly Matched Layers . . . . .           | 41        |
| 4.3      | Unit Cell Simulations . . . . .   | 44        |
| 4.3.1    | Simulation Considerations . . . . .                                       | 44        |
| 4.3.2    | Effects of Lattice Parameter $a$ and Cell Tether size $w$ . . . . .       | 47        |
| 4.4      | Flower and Web Designs . . . . .  | 50        |
| 4.4.1    | Characterizing a Bandgap in COMSOL . . . . .                              | 52        |
| 4.4.2    | Flower . . . . .  | 56        |
| 4.4.3    | Web . . . . .   | 58        |
| <b>5</b> | <b>Modeling Optical Absorption for <math>\text{Si}_3\text{N}_4</math></b> | <b>62</b> |
| 5.1      | Introduction . . . . .  | 62        |
| 5.2      | Heat Equation Modeling . . . . .  | 63        |
| 5.3      | Cryogenic Thermal Conductivity Values . . . . .                           | 66        |
| 5.4      | Lower-bounds on Optical absorption . . . . .                              | 70        |
| 5.4.1    | 1064nm light at Milikelvin Temperatures . . . . .                         | 70        |
| 5.4.2    | 1064nm light at Cryogenic Temperatures . . . . .                          | 72        |
| 5.4.3    | 904nm light at Milikelvin Temperature . . . . .                           | 72        |
| 5.4.4    | 850nm Tether Heating . . . . .  | 75        |
| <b>6</b> | <b>Conclusion</b>   | <b>79</b> |
|          | <b>Bibliography</b>   | <b>81</b> |

## Tables

### Table

|     |   |    |
|-----|---|----|
| 4.1 | Calculated Qs for membrane with PML COMSOL model. . . . .   | 42 |
| 4.2 | Geometric parameters of Tsaturyan et al. unit cell depicted in figure 4.3. . . . .                  | 44 |
| 4.3 | The parameters necessary to define the basis of the k-space for the unit cell in Fig. 4.3. . . . .  | 47 |
| 4.4 | Mode Q Ratios for the Membrane-Defect PnC. . . . .  | 56 |
| 5.1 | Parameters of the Heat Equation. . . . .  | 64 |
| 5.2 | Thermal Conductivity Expressions for SiN at mK Temperatures. . . . .                                | 69 |
| 5.3 | Thermal Conductivity Values for SiN at Cryogenic Temperatures. . . . .                              | 69 |
| 5.4 | Heating of Si <sub>3</sub> N <sub>4</sub> at Milikelvin Temperatures. . . . .                       | 72 |
| 5.5 | Wilson et al. tether parameters [40]. . . . .   | 77 |
| 5.6 | Summary of the Calculated Optical Absorption Minima for Different Experimental Data Points. . . . . | 78 |

## Figures

### Figure

|      |  |    |
|------|--|----|
| 2.1  | Diagram of a Fabry-Pérot cavity with movable mirror, the archetypical cavity optomechanics system. . . . . | 8  |
| 2.2  | Modulation of the input laser light by a movable mirror in an optical cavity. . . . .                      | 10 |
| 2.3  | Illustration of a membrane-in-the-middle cavity optomechanics system. . . . .                              | 14 |
| 2.4  | Diagram of a $\text{Si}_3\text{N}_4$ membrane-in-the-middle cavity in a He Cryostat. . . . .               | 16 |
| 2.5  | Diagram of a Hybrid Electro-, Optomechanics Cavity Experiment . . . . .                                    | 17 |
| 2.6  | Diagram of an MRFM Experiment Using a Cantilever. . . . .  | 19 |
| 2.7  | Diagram of an MRFM Experiment Using a Membrane. . . . .  | 20 |
| 3.1  | Energy Stored in Elongation and Bending as a Function of Stress for a SiN string. . . . .                  | 25 |
| 3.2  | Bending of a SiN String Close to the Clamping Edge. . . . .  | 25 |
| 3.3  | Effects of the Geometry of the Connection Between Resonator and Substrate. . . . .                         | 27 |
| 3.4  | 1D chain of equal masses connected by springs. . . . .   | 28 |
| 3.5  | Dispersion Relation for a 1D Chain of Equal Masses. . . . .  | 30 |
| 3.6  | 1D chain with Alternating Spring Constants. . . . .  | 30 |
| 3.7  | Dispersion Relation for a Unidimensional Chain with Two Degrees of Freedom. . . . .                        | 31 |
| 3.8  | Picture of Phononic Crystal Substrate for a $\text{Si}_3\text{N}_4$ membrane. . . . .                      | 33 |
| 3.9  | Dispersion Relation for Yu et al. Silicon Phononic Crystal. . . . .  | 34 |
| 3.10 | Membrane and Si PnC crystal Mode Decoupling. . . . .   | 35 |

|      |   |    |
|------|---|----|
| 3.11 | SI <sub>3</sub> N <sub>4</sub> Trampoline Geometry. . . . .   | 36 |
| 3.12 | SI <sub>3</sub> N <sub>4</sub> Phononic Crystal Design. . . . .   | 37 |
| 3.13 | SI <sub>3</sub> N <sub>4</sub> PnC Dispersion Relation. . . . .   | 38 |
| 3.14 | Attenuation and Curvature of a Defect Mode in Band-gap of the SI <sub>3</sub> N <sub>4</sub> PnC. . . . . | 39 |
| 4.1  | COMSOL Model of a Membrane External Loss via PML. . . . .   | 43 |
| 4.2  | COMSOL membrane and PML 22 mode. . . . .  | 43 |
| 4.3  | Picture of Phononic Crystal Substrate for a Si <sub>3</sub> N <sub>4</sub> membrane. . . . .              | 45 |
| 4.4  | Floquet Periodic Boundaries in the Unit Cell. . . . .   | 46 |
| 4.5  | Unit Cell Symmetry Points for the Calculation of Stress. . . . .  | 48 |
| 4.6  | Calculated Stress-Distribution of the Unit Cell. . . . .  | 48 |
| 4.7  | Dispersion Relation Simulation for the Unit Cell. . . . .   | 49 |
| 4.8  | Bandgap Dependence on Cell Tether $w$ Size for $a = 160\mu\text{m}$ . . . . .                             | 51 |
| 4.9  | Bandgap Dependence on Cell Tether $w$ Size for $a = 67\mu\text{m}$ . . . . .                              | 51 |
| 4.10 | PnC Domains Used in Finding the Energy Ratio $E_r$ . . . . .  | 53 |
| 4.11 | COMSOL Results for In-Bandgap Defect Mode and Non-Defect Mode. . . . .                                    | 54 |
| 4.12 | Energy Ratios for membrane-PnC . . . . .  | 55 |
| 4.13 | Flower Trampoline-Defect PnC Design . . . . .   | 57 |
| 4.14 | Energy Ratios for Flower-PnC with 11x19 cells . . . . .   | 57 |
| 4.15 | Energy Ratios for Flower-PnC with 5x9 cells . . . . .   | 58 |
| 4.16 | Web Trampoline-defect PnC design . . . . .  | 59 |
| 4.17 | Energy Ratios for Web-PnC with 11x19 cells . . . . .  | 60 |
| 4.18 | Energy Ratios for Web-PnC with 5x9 cells . . . . .  | 61 |
| 4.19 | Energy Ratios for Web-PnC with 9x15 cells . . . . .   | 61 |
| 5.1  | Energy Balance of a 2D Infinitesimal Membrane Element Illuminated by a Gaussian Beam. . . . .             | 63 |
| 5.2  | Energy Balance of a 1D Infinitesimal tether Element Illuminated by a Gaussian Beam. . . . .               | 65 |

|      |  |    |
|------|--|----|
| 5.3  | Thermal Conductivity of Amorphous Solids. . . . .  | 68 |
| 5.4  | Thermal Conductivity of Low and High Stress SiN. . . . .   | 69 |
| 5.5  | Experimental setup of Quantum Backaction Limit Experiment. . . . .   | 70 |
| 5.6  | Maximum Temperature on Membrane vs. Optical Power at for 1064nm light at<br>Milikelvin Temperatures. . . . . | 71 |
| 5.7  | Maximum Temperature on Membrane vs. Optical Power at for 1064nm light at<br>Cryogenic Temperatures. . . . .  | 73 |
| 5.8  | 904nm Optical Absorption Experiment at Milikelvin Temperature. . . . .                                       | 74 |
| 5.9  | Temperature distribution on Membrane for 904nm light at Milikelvin Temperatures.                             | 75 |
| 5.10 | Tether Whispering Gallery Geometry. . . . .  | 76 |
| 5.11 | Tether Temperature as a Function of Cryostat Temperature for Tether. . . . .                                 | 77 |
| 5.12 | 1D Model Results for the Heating of a Trampoline with 850nm. . . . .   | 78 |

# Chapter 1

## Introduction

### 1.1 Context

The 20<sup>th</sup> century saw the emergence of quantum mechanics as a highly successful theory able to explain with high success diverse microscopic phenomena. The inability of classical mechanics and electrodynamics in explaining black-body radiation led to the introduction of the *quantization* of light by Planck and later Einstein, who postulated the corpuscular facet of light waves. De Broglie expanded this duality by postulating that all matter has wave properties, with characteristic wavelengths inversely proportional to momenta. The wave-like behavior of matter was later enshrined by Schrödinger's wave equation, which ascribes behavior typical of waves, such as superposition and interference, to the probability density of the properties microscopic entities. Since then, the predictions made by Schrödinger's equation and the rest of quantum mechanics have been confirmed countless times and to exquisite degrees of accuracy and precision.

Nonetheless, at the same time that superposition and interference have been incorporated with great success in the behavior of particles, its existence in the case of macroscopic, large-mass systems still remains mysterious and, as such, a forefront topic of exploration in physics. Moreover, the refined technical control of mechanical systems achieved in the last few decades is now encroaching what used to be firmly classical fields, and the developed quantum control is now expected to expand to ever-massive systems and system with larger. For example, the recently successful observation of gravitational waves [1] was only possible after taking into account the quantum behavior of the kg-mirrors at the end of the km-long interferometer arms of LIGO [2].

This example is a particular and case of of the larger field of *Cavity Optomechanics*, which more often brings together advances in micro-fabrication and quantum optics. The sophisticated nanofabrication techniques developed by the semiconductor industry have allowed for the development of mechanical sensor capable of probing very small forces, as exemplified in scanning-force microscopy. At the same time, developments in quantum optics have clarified light-matter interactions and the ultimate limits quantum mechanics impose on mechanical sensing, a consequence of the back-action caused by quantum measurement [2, 3]. Cavity Optomechanics seeks to use this quantum back-action to manipulate the mechanics of suitable resonator, many micro-fabricated, ultimately achieving “quantum control of [their] mechanical motion [3].”

The quantum behavior of a system can be more readily observed when its number of quanta of oscillation, called *phonons*, is small [2]. In fact, for an oscillator such as a micro-mechanical resonator its number of phonons is the fraction of its mean thermal energy and a quantum of oscillation. Thus, if the temperature of a resonator is drastically reduced such that its thermal energy is much smaller than that of a phonon, the quantum behavior of the resonator can be finally accessed. In cavity coupling the mechanical oscillator motion with the fundamental modes of trapped light inside a cavity is capable of realizing this drastic cooling to the quantum regime.

One can understand the physical principle behind Cavity Optomechanics by considering a Fabry-Pérot cavity, formed by two mirrors facing each other, with one of the mirrors allowed to oscillate in harmonic motion [3]. For a Fabry-Prot cavity with rigid mirrors, white light introduced into the cavity will reflect back and forth and interfere with itself, and only those frequencies  $\omega_c$  compatible with the modes of the cavity will interfere constructively and remain trapped in the cavity. If, however, one of the end mirrors can oscillate with frequency  $\omega_m$ , then the trapped light will be modulated into two frequencies  $\omega_c \pm \omega_m$ . Photons of frequency  $\omega_c + \omega_m$  are *blue-shifted* and remove energy from the mechanical oscillator, whereas photons of frequency  $\omega_c - \omega_m$  are *red-shifted* and add energy to the mechanical oscillator. If the incoming light is a laser beam with frequency  $\omega_L = \omega_c$ , then the modulation will be symmetric and the resonator’s energy won’t change. However, if the incoming light is slightly red detuned, i.e.,  $\omega_L = \omega_c - \Delta$ , then the blue shifted photons can

be put in resonance with the cavity, since their frequency can be closer to  $\omega_c$ . This way, the blue-shifted light will take energy out of the resonator, causing it to cool down. If the mirrors of the cavity have very high finesse, that is, if light trapped in the cavity can be reflected many times before eventually leaking out, the cooling process will be enhanced and very low phonon number can be achieved, leading the resonators to the quantum regime [2, 3].

In practice, there are different setups that can achieve optomechanical cooling. For instance, reflective cantilevers and high-finesse mirrors can directly implement the model discussed previously, and ultracold atoms, microspheres, and membranes can be placed inside a cavity and have their motion be modulated by incoming light. At lower frequencies, metallized membranes can be coupled to electromagnetic resonators by forming one of the plates of a capacitor in a superconducting LC circuit. Alternatively, waveguides can be used as “whispering gallery” resonators that can trap light waves which causes oscillatory “breathing modes” coupled to the modes of the trapped light. Finally, kilogram-sized movable mirrors can be placed at one end of kilometer sized cavities, as is done in LIGO, whose quantum back-action limited resolution led to theoretical development of optomechanics.

Even though the motivation of cavity optomechanics is to reach quantum control of mechanical motion, research on its different realizations indicates possible applications in, for example, force-sensing, displacement measurement, NMR, and signal conversion. Intuitively, the less thermal fluctuation a device has, i.e., the more it stands still, the more pronounced its response to an external force will be. In other words, if thermal fluctuations are making a mechanical device jitter randomly, any displacement smaller than the jitter’s amplitude (say, a displacement resulting from a very small external force), will remain undetected. Therefore, by greatly reducing the thermal fluctuations of mechanical detector, one can increase its sensitivity to external forces and displacements. Moreover, if the mechanical structure is coupled to two cavities of different resonant frequencies, the sensitivity of each cavity to signals from the other is likewise enhanced if their shared resonator has been cooled down.

In the Regal lab, cavity optomechanics has been pursued successfully both in basic quantum

mechanics research and in more applied endeavors. In the group’s experiments, a stoichiometric (high-stress) silicon nitride ( $\text{Si}_3\text{N}_4$ ) membranes is positioned in the middle of a high-finesse, rigid Fabry-Pérot cavity [4], which is inserted in either a cryostat or a dilution refrigerator for preliminary cooling of the cavity and membrane to cryogenic ( $< 5K$ ) temperatures, with further cooling accomplished by using laser-cooling techniques. Using this setup, the Regal lab has observed the shot noise back-action on the membrane due to the trapped light and squeezing of light due to optomechanical interactions, both purely quantum effects. Moreover, by depositing superconducting metal on part of the  $\text{Si}_3\text{N}_4$  membrane and using it as a capacitor plate in an LC circuit, the group has also achieve improved microwave-to-optical photon conversion rates [5]. Further experiments have reached the back-action limit [6], and improvements in the performance of the membrane resonators will allow the trend of successful experiments to continue.

In fact, an obvious limitation to the performance of  $\text{Si}_3\text{N}_4$  membrane resonators is its optical absorption properties. If the membrane converts too much of the incoming light into heat, laser cooling will be very limited [7]. Fortunately, very low optical absorption have been inferred for silicon nitride membranes [8]. Nonetheless, a precise measurement of the optical absorption and the thermal conductivity of  $\text{Si}_3\text{N}_4$  membrane has not yet been achieved.

A more relevant parameter for the resonators used in cavity optomechanics, membranes included, is their quality factor  $Q$ , i.e., the ratio between total energy stored and energy loss per oscillation. In fact, higher  $Q$  correspond to better coupling and more efficient and extensive cooling, and it also allows for higher frequency measurements and greater sensing capabilities [9]. Therefore, by reducing the losses of a resonator and consequently improving its  $Q$ , experiments can more easily achieve the quantum regime for the resonators, and improve sensing resolutions.

The losses of a  $\text{Si}_3\text{N}_4$  resonator can be divided into external and internal losses. The former is due to phonon tunneling to the substrate, i.e., energy lost to the substrate [10, 11]; the latter happens because energy is lost whenever bending of the silicon nitride occurs [12, 13, 14]. In work done by Yu et al. [15], the silicon substrate of a  $\text{Si}_3\text{N}_4$  membrane was patterned into a phononic crystal (PnC) structure in order to obtain a “phononic” bandgap, which prevents acoustic

waves with frequencies within the bandgap to propagate through the silicon substrate. Thus, if a membrane has a mode frequency within the bandgap, that mode's  $Q$  will be enhanced by reducing its external losses to the substrate. More recently, two groups have demonstrated that patterning the  $\text{Si}_3\text{N}_4$  resonator into “tethered membranes” could reduce both internal and external losses [16, 17] by, respectively, a combination of higher stress at the tethers connecting the membrane to the substrate [13], and by reducing the contact area between membrane and substrate to only the cross-sectional area of the tethers [11]. This loss reduction has resulted in room-temperature  $Qf$  product an order of magnitude higher than for a regular high-stress membrane at cryogenic temperatures. Nonetheless, another approach has proven even better at reducing the losses: patterning a (PnC) directly in the  $\text{Si}_3\text{N}_4$  resonator, with a central, un-patterned defect taking the role of the membrane [18]. The  $\text{Si}_3\text{N}_4$  PnC decouples substrate and defect modes, which drastically reducing external loss, and it also reduces bending close to the substrate where they are specially lossy [14]. The reduced losses and higher  $Q$  these designs have achieved will enable new experiments in both basic and applied optomechanics research.

In particular, the Regal lab seeks to use trampoline geometries in magnetic resonance force microscopy (MRFM), in an improvement of experiments done by other groups with low stress SiN membranes [19]. Additionally, the use of tethered geometries can also be used for polarizing of spins [20]. In parallel, the group also seeks to combine trampoline and  $\text{Si}_3\text{N}_4$  PnC structures to obtain high performing resonators which are also optimized for the detection of spins. By having a trampoline as defects, instead of a membrane, the effective mass of the resonator can be decreased, which improves its sensing capabilities [17], and the defect tethers can also be used in spin detection and polarization experiments.

## 1.2 Outline

Chapter 2 of this thesis delves in the basic theory of cavity optomechanics and briefly discusses some of the applications being studied by the Regal group. We then move on to chapter 3 to go over the limitations to high-stress  $\text{Si}_3\text{N}_4$  membrane resonators, starting with some of the theory

behind internal and external losses. The next section explains the solid-state theory necessary for a basic understanding of phononic bandgaps and how it can be used for PnC crystals. Finally, the chapter ends with a discussions of the effects of optical heating, and why we care about it.

The next two chapters discuss my work and results studying optical absorption and hybrid trampoline-PnC resonator geometries. Chapter 4 explains further the merits of the  $\text{Si}_3\text{N}_4$  PnC resonators, and relates a couple new hybrid trampoline-PnC designs. This chapter also contains a few of the most important considerations in simulating such structures using the finite-element software COMSOL. Chapter 5 discusses how optical heating models were used in determining upper bounds to experimental data, providing initial corroboration that  $\text{Si}_3\text{N}_4$  has an extremely low optical absorption figure.

The final chapter is a short conclusion which recaps the material discussed and discusses a few of the possible directions for extending the work related in this thesis.

## Chapter 2

### Cavity optomechanics

#### 2.1 Basic Theory of Cavity Optomechanics

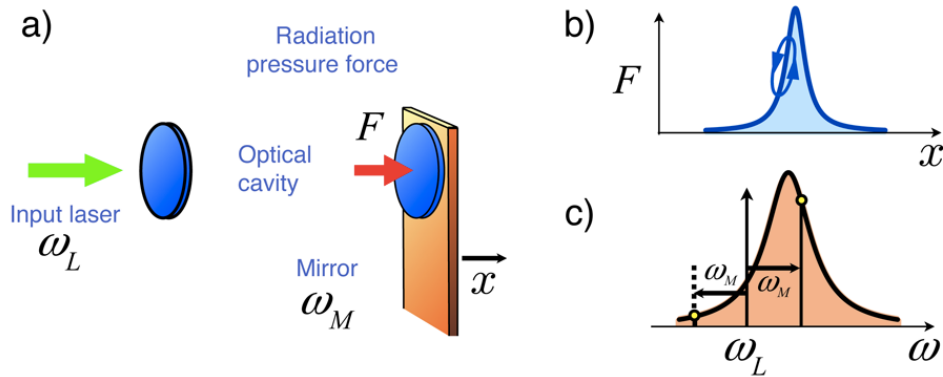
As is common in many introductions [2, 3, 21], let's consider the archetypical optomechanical system: a Fabry-Pérot optical resonator with one of its end mirrors capable of oscillating harmonically. When monochromatic laser light of frequency  $\omega_L$  is inserted into the cavity, it will reflect back and forth, exerting a force  $F_{\text{rp}} = 2P_{\text{opt}}/c$  upon reflection (Fig. 2.1(a)). This will cause the movable mirror to be displaced and start oscillating, which will change the frequency  $\omega_c = mc/L$  of optical modes of the cavity. The resulting shift of  $\omega_c$  will either position the laser light frequency  $\omega_L$  closer or farther away from resonance, which will cause it to reflect less or more, respectively, inside the cavity, decreasing or increasing  $F_{\text{rp}}$ . In fact, as described below, it is precisely the coupling of the optical field with the mechanical motion of the mirror due to the radiation pressure force  $F_{\text{rp}}$  that enables all aspects achieved by cavity optomechanics.

In particular, the radiation pressure mediated coupling results in an “optical spring effect,” not discussed in this thesis (see [3] and [21] for more information), and “optical damping”, which leads to the the possibility of laser cooling the resonating mirror to the quantum regime.

Optical damping can be explained classically by taking into account the delay in the response of the radiation pressure force to the induced displacements of the mirror [2, 21]. Let's reconsider the Fabry-Pérot cavity from above. According to Marquardt and Girvin, the force exerted on the on the mirror by radiation pressure is a Lorentzian with respect to the mirrors displacement  $x$  [21], as seen plotted in Fig. 2.1(b). Suppose that initially the mirror is positioned to the left of

the resonance peak. Either the radiation pressure force or random thermal fluctuations will make the mirror oscillate and move with respect to the Lorentzian. Let's assume it moves closer to the resonance peak. Now, before the radiation pressure force can “catch up” with the mirror and increase its magnitude, all the old, “weaker” photons need to leak out of the cavity. Therefore, in moving towards the resonance the mirror will feel a smaller force than it would if the radiation pressure force corrected instantaneously, which reduces the work exerted by the field on the mirror. However, as the mirror oscillates back from the resonance, the force will then be larger than it would be without the time-delay, which will make the mirror exert more work against the optical field than otherwise expected. Overall, the radiation pressure force will remove work from the mirror, effectively cooling it down, damping its motion [21].

Figure 2.1: **(a)** Illustration of a Fabry-Pérot optical cavity with one end-mirror attached to a movable cantilever with oscillation frequency  $\omega_M$ . The input laser light of frequency  $\omega_L$  exerts a radiation pressure force  $F = 2P_{\text{opt}}/c$  onto the mirror, which is displaced along  $x$ . **(b)** Plot of the Lorentzian describing the radiation pressure force  $F$  exerted on the movable mirror as a function of the mirror's displacement  $x$ . For a mirror initially positioned to the left of the peak force magnitude, an oscillation cycle takes away energy from the mirror. **(c)** If incoming light is slightly red-shifted compared to the cavity resonance, the modulated band of frequency  $\omega_L + \omega_M$  is closer to the resonance and its process is therefore more efficient. Since that band corresponds to the negative-work process, the oscillating mirror is damped more efficiently. (Image credit: Marquardt and Girvin [21]).



Clearly, if the mirror is positioned on the opposite side of the Lorentzian of the radiation pressure force, energy will be given to the mirror and it will heat-up. To better understand how optical damping can be selected for in a cavity, let's consider the quantum mechanical picture.

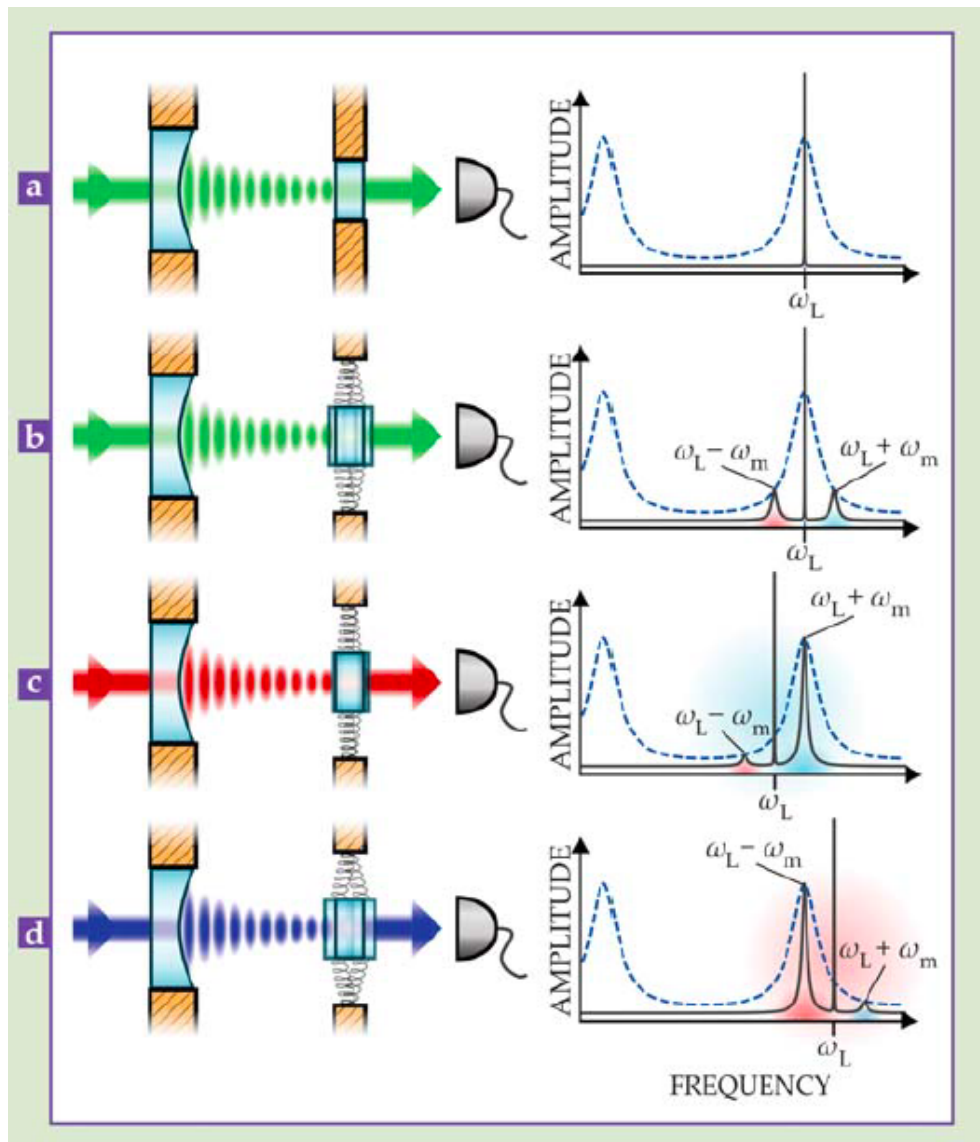
Incoming laser light of  $\omega_L$  consists of a stream of photons of energy  $E = \hbar\omega_L$  whose total number is determined by the laser input intensity. If the cavity has both mirrors fixed, then the photons will stay inside the cavity longer the closer their frequency  $\omega_L$  is closer to the cavity resonant frequency  $\omega_c$ , and the leaked light intensity will be the highest when  $\omega_L = \omega_c$  (Fig. 2.2(a)). Now, if the end mirror can oscillate, when the photons hit it they can either create or destroy a phonon of energy  $\hbar\omega_M$ . Clearly, if a phonon is created, then the energy of the mirror increases by an additional  $\hbar\omega_M$  (a phonon), and the reflected photon is red-detuned to a lower energy  $\hbar(\omega_L - \omega_M)$ . If a phonon is destroyed, then the energy of the mirror is decreased by  $\hbar\omega_M$  and the reflected photons is blue-shifted to a higher energy  $\hbar(\omega_L + \omega_M)$ . This modulation is equally distributed about the input frequency  $\omega_L$  and both blue- and redshifted light leak to the outside (Fig. 2.2(b)). However, by slightly red-detuning the incoming light, the redshifted light can be pushed far from resonance, whereas the blueshifted can be placed in resonance with the cavity, which would enhance phonon destruction (Figs. 2.1(c), 2.2(c)). The opposite process occurs if the input light is blue-detuned, enhancing phonon creation at the mirror (Fig. 2.2(d)).

The mirror's quantum regime can be accessed if its thermal fluctuations are small enough that they don't wash out the observable effects from small quanta of motion or energy. Thus, the optical damping has to remove enough thermal phonons from the mirror such that on average less than one thermal phonon will be present [2]. In other words, let  $\bar{n}$ , the occupation number, be the average number of thermal phonons in the mirror. The cooling provided by optical damping has to achieve

$$\bar{n} \approx \frac{k_b T}{\hbar\omega_M} < 1$$

which means that the mean thermal energy  $k_b T$  has to be smaller than a quantum of mechanical energy, achieving an occupation on average less than 1. This can be achieved provided the cavity resonance linewidth (the width at half maximum at the resonance at Fig. 2.1(c)) is smaller than the separation  $2\hbar\omega_M$  between the two modulation bands [21]. The smaller the resonance linewidth is compared to the band separation, the greater the rate of cooling compared to heating for a red-

Figure 2.2: (a) A Fabry-Pérot rigid cavity with input laser light of frequency  $\omega_L = \omega_c$ . The resonance increases the intensity of the light in the cavity, amplifying the output signal. (b) If one of the mirrors is allowed to oscillate harmonically with frequency  $\omega_m$ , the input is modulated into two bands of frequency  $\omega_L - \omega_m$  and  $\omega_L + \omega_m$ . The former gives energy to the mirror, adding a phonon of energy  $\omega_m$  and the latter subtracts energy from the mirror by destroying a phonon. (c) If the input light is red-detuned such that the blue-shifted, the phonon destroying process is selected for by the cavity resonance, which greatly dampens the motion of the mirror. (d) If the input light is blue-detuned, the phonon creating process is the one selected, which increases the energy of the mirror. (Image credit: Aspelmeyer et al. [2]).



detuned input. It also becomes clear that the number of incoming photons has to be high enough such that the phonon-destroying process happens at a faster rate than that of thermal phonons entering the mirror from the outside [21]. If the cavity resonance is good enough and if the sources of thermal phonons from the outside is negligible, the optical damping can be strong enough to reveal the mirrors quantum behavior.

Despite the apparent lack of generality of the system discussed above, the physics involved is generic enough that it can be extended to different systems, all capable of realizing cavity optomechanical cooling. According to Marquardt and Girvin argue:

On the most general level, we are dealing with a resonance (the optical cavity mode) that is driven (by a laser), and whose resonance frequency is pulled by the displacement of some mechanical degree of freedom (the movable mirror). Having the resonance frequency depend in this manner on the position immediately implies that there will be a mechanical force. Given this general description, it is no wonder the same physics has by now been realized in a diverse variety of physical systems, including superconducting microwave circuits and ultracold atoms [21].

In the model discussed above, the resonance frequency is coupled to the position of the moving resonator (mirror), which is oscillating due to the radiation pressure force. Larger forces result in stronger coupling, as the effects on the resonance will be more pronounced. We can then derive our first merit figure for optomechanical systems in general based on this fact. The radiation pressure force on reflection from the mirror is given by

$$F = \hbar \frac{\omega_c}{L} \bar{n}_{\text{cav}} \quad (2.1)$$

where  $G = \omega_c/L$  is the change of resonance frequency with position parameter and  $\bar{n}_{\text{cav}}$  is the number of photons in the cavity, which is proportional to the laser intensity. We can move further and define a *vacuum optomechanical strength*, which indicates how strongly a photon interacts with the phonons in the resonator:

$$g_0 = G x_{\text{zpf}} = \frac{\omega_c}{L} \sqrt{\frac{\hbar}{m_{\text{eff}} \omega_M}} \quad (2.2)$$

where  $x_{\text{zpf}}$  is the zero point motion of the resonator, which is the position expectation value of a harmonic oscillator in its ground state. The vacuum optomechanical coupling strength then indicates that the larger a resonator's  $x_{\text{zpf}}$ , the stronger the coupling between its phonons and the

cavity's photons. Notice that the couplings  $G$  and  $g_0$  have units of frequency, so intuitively we want the interaction rates denoted  $g_0$  to be larger than any dissipation rate due to the environment. In this way, the optomechanical processes discussed above can happen faster than the system thermalizes and interacts with its surrounding.

Independent of the physical system, we can now understand the role of the mechanical oscillator's performance in achieving optomechanical cooling. A mechanical resonator with an oscillating mode of frequency  $\omega_M$  will lose mechanical energy at a damping rate  $\Gamma_M$ , which relates to its *quality factor* by the expression  $Q_M = \omega_M/\Gamma_M$ . In contact with a thermal bath with average thermal occupation  $\bar{n}_{th}$ , the motion of the mechanical oscillator will dampen according to the change in its average phonon occupation  $\bar{n}$  [22]:

$$\frac{d}{dt}\bar{n} = -\Gamma_M(\bar{n} - \bar{n}_{th}) \approx \frac{\omega_M}{Q_M}(\bar{n} - \frac{k_b T}{\hbar\omega_M}) \quad (2.3)$$

Where the right-most equality uses the high-temperature approximation  $\bar{n} \approx k_b T/\hbar\omega_M$ . Notice that once the mechanical resonator has an average occupation number equal to zero, that is, it is in its ground state corresponding to  $\bar{n} \rightarrow 0$ , equation 2.3 implies that it will receive thermal phonons from the surroundings at a rate inversely proportional to the resonator's quality factor:

$$\frac{d}{dt}\bar{n} \approx \frac{k_b T}{\hbar Q_M} \quad (2.4)$$

Equation 2.4 is referred as the *thermal decoherence* rate and it denotes the rate by which one quantum of energy is gained from the environment. Clearly, the maintenance of quantum behavior for a mechanical resonator that has been cooled down to its ground state depends on low thermal decoherence, which occurs for high quality-factors and is likewise improved by low thermal bath temperatures. Moreover, the product  $Qf$  of a mechanical resonator can quantify how decoupled the system is from the thermal bath [22]. Consider the ratio between the frequency of a mode to the thermal decoherence:

$$\frac{\omega_M}{\bar{n}_{th}\Gamma_M} = \frac{Q_M}{k_bT/\hbar\omega_M} = Q_M f_M \frac{h}{k_bT} \quad (2.5)$$

The ratio is directly proportional to the  $Q_M f_M$  product, which means more oscillations will occur given a particular thermal decoherence, i.e., the mechanical resonator is less coupled to its environment and can be cooled down and maintained cold more effectively.

## 2.2 Membrane-in-the-middle Systems

The actual implementation of a Fabry-Pérot cavity with a movable end-mirror is limited because reflectivity, which increases the light intensity in the cavity, and pliability, which relates to the quality factor, are almost always incompatible in the same material <sup>1</sup>. One way of addressing this limitation is, for example, to physically separate the mechanical and optical properties of the system by having a partially translucent membrane in the middle of a rigid mirrors cavity (2.3(a)) [8]. In such setups, the membrane divides the cavity optical field into two, both modulated by the oscillatory-mode shape of the membrane. Regardless of this difference, the generalization of the model of section 2.1 holds, and, in this way, pursuing higher quality factors for the membrane can be done without detriment to the reflectivity of the cavity, which is determined by the mirrors alone.

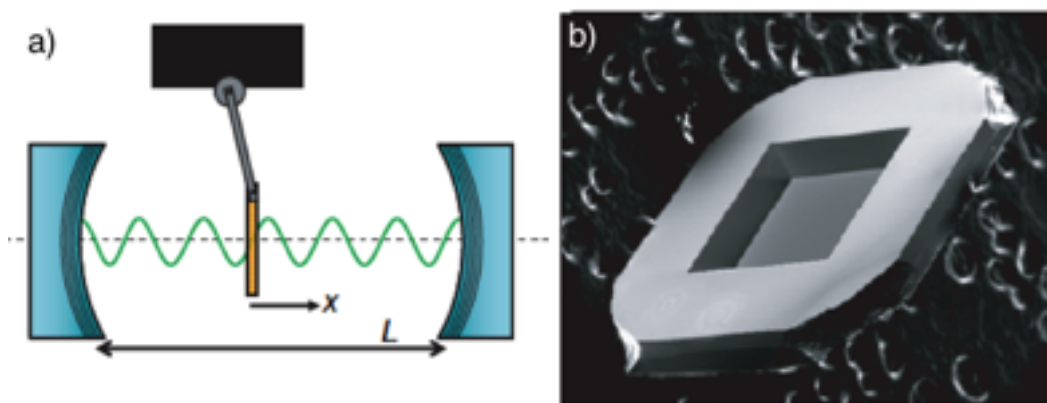
In particular, silicon nitride (SiN) membranes (Fig. 2.3(b)) have shown promise in membrane-in-the-middle setups. Their low-stress variant have been measured to have near-IR absorption of less than  $10^{-4}$ , an important parameter in avoiding enhancing the laser-cooling described in section 2.1, since it would be counter-productive to have the laser adding thermal phonons to the membrane at an appreciable rate. More impressively, their measured quality factors have exceeded  $10^6$  at room temperature, two orders of magnitude larger than cantilevers used in atomic force microscopes [7]. The combination of these two parameters have allowed SiN membrane systems to achieve temperatures much lower than those achieved by systems using reflective cantilevers. For example, whereas Thompson et al. reported achieving 6.82mK using a membrane in the middle system [23]

---

<sup>1</sup> with an exception presented in Norte et al. [16].

a cantilever cavity approach implemented by Corbitt et al. was capable to cool a 1g cantilever-like structure to 0.8K [24], more than a 100 times the temperature obtained using the membrane.

Figure 2.3: (a) An schematic representation of a membrane in the middle system. The membrane light trapped in the cavity exerts a force on the membrane, displacing it along  $x$ . Instead of depicting the sinusoidal modes of the membrane, the membrane oscillation is representing by a movable lever. As the membranes moves, it changes the length of the cavity in either of its sides, coupling its motion to the trapped light through radiation pressure (as discussed in section 2.1). (b) A photograph of a SiN membrane and its Si substrate. Such a membrane have superior quality factor compared to cantilevers, and if used with high-reflectivity mirrors, result in better optomechanical cooling. (Image credits: Thompson et al [23]).



## 2.3 Silicon Nitride Membrane Experiments

### 2.3.1 Observation of Quantum Behavior

Compared to the low-stress SiN membranes described in section 2.2, high-stress silicon nitride membranes ( $\text{Si}_3\text{N}_4$ ) have a larger tensile stress of around 1GPa, which, up to dimension differences, results in larger mode frequencies, which necessarily improves its  $Qf$  product. Moreover,  $\text{Si}_3\text{N}_4$  membranes seem to have even lower near IR optical absorption [25], as discussed in chapter 5. According to the discussion of section 2.1, both improvements would make it a better mechanical element at a cavity optomechanical experiment than a low-stress SiN membrane, itself a better performing resonator than cantilevers (Fig. 2.3(b)).

These high-stress membranes have been used in the Regal lab with a He flow cryostat to

reveal their intrinsic quantum behavior [4]. With good insulation from a radiation shield and a cold window, the  $\text{Si}_3\text{N}_4$  can thermalize to the Cryostat temperature of  $4.2\text{K} < 300\text{K}$  (Fig. 2.4), which greatly decreases the thermal decoherence to which it is subjected (eq. 2.4). In addition, the thermal decoupling is further enhanced by the high-stress membrane's improved  $Qf$ . These features have allowed the group to observe the back-action on the membrane from radiation pressure, which occurs when  $\bar{n} < 1$  and the photon induced movements become more prominent [26]. Further studies led to "optomechanical squeezing of light," another purely quantum effect [27], and to the quantum back-action cooling limit [6].

### 2.3.2 Conversion Between Optical and Microwave Signals

Another experiment that takes advantage of the improved parameters of  $\text{Si}_3\text{N}_4$  membranes seeks to have a quantum-state preserving conversion between microwave and optical signals. The setup consists of both the discussed Fabry-Pérot cavity with a high-stress silicon nitride membrane in the middle and a microwave cavity formed by a superconducting LC circuit, the archetypical cavity in *electromechanics*, the microwave-frequency equivalent of optomechanics. The two cavities are coupled by having a part of the membrane coated with niobium, which superconducts below  $9\text{K}$ . The uncoated part of the membrane modulates the optical cavity frequency of the system, whereas the coated surface forms the top plate of the capacitor in the LC circuit (Fig. 2.5(a) and (b)). The membrane oscillations will then not only modulate the trapped light, but also the resonant frequency of the circuit [5].

Using a dilution refrigerator which reduces the thermal bath temperature below  $40\text{mK}$ , this hybrid system was capable of almost "noiseless frequency conversion" between microwave and optical photons, with a photon number efficiency of  $0.086 \pm 0.007$ , an efficiency that can be improved by using membranes or resonators with larger quality factors [5]. In order to make a link between two cavities operating at different frequencies, both have to be pumped with red-detuned light (Fig. 2.5(c)), which cools down the mechanics and enables a signal to be converted between the two characteristic frequencies [5].

Figure 2.4: (a) A Diagram of  $\text{Si}_3\text{N}_4$  in a He Cryostat used in some of the experiments in the Regal lab. The Fabry-Pérot cavity is formed by a curved and a flat mirror, with the high-stress silicon nitride membrane positioned in between the two. The mirrors are affixed into an invar support, which is thermally connected to the He flow cryostat, and is protected by a radiation shield, a vacuum shroud, and a cold window, all of which improve the cavity's isolation from the surrounding environment (Image credits: Purdy et al. [4]).

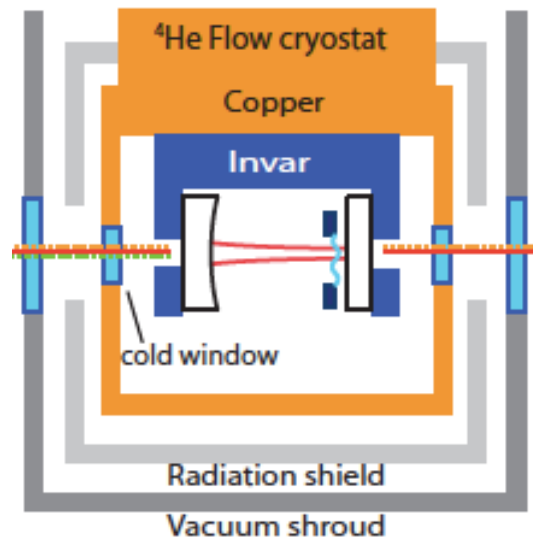
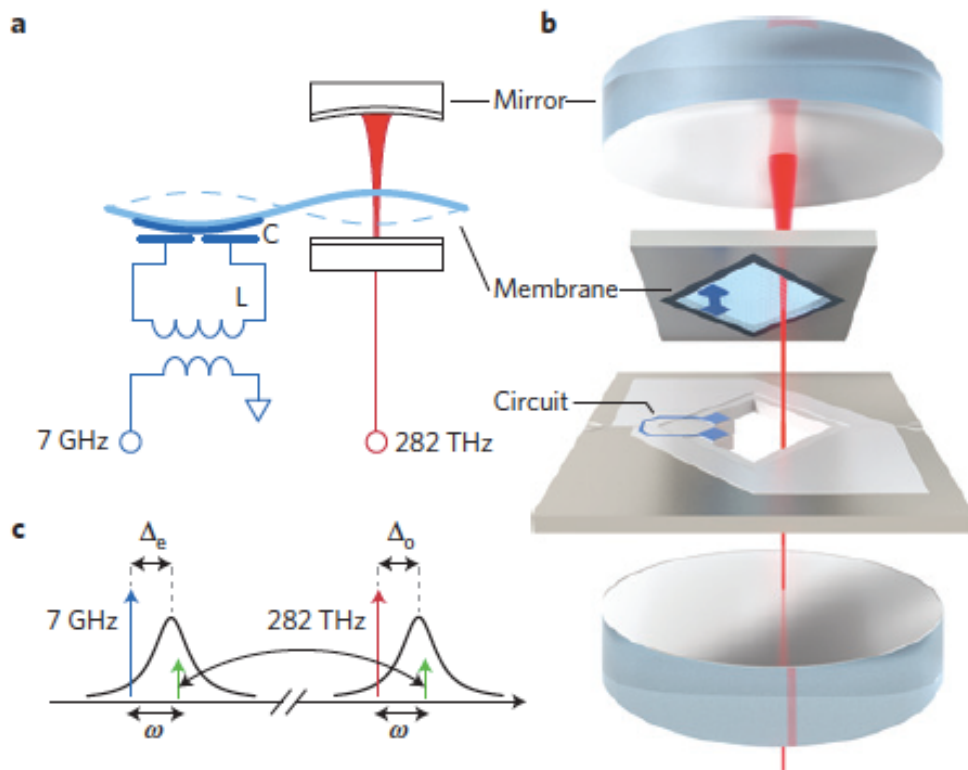


Figure 2.5: **(a)** Schematic of the hybrid setup which uses a  $\text{Si}_3\text{N}_4$  membrane to mediate between an optical and a microwave cavity. The membrane is partially coated in niobium (dark blue), which forms the top plate of a capacitor on a superconducting LC circuit, which modulates its resonant frequency in the same fashion as its uncoated part modulates the optical cavity frequency. **(b)** An illustration of the setup, with the flip-chip assembly composed of a top chip containing the partially metallized membrane and the bottom chip containing the rest of the circuit. The flip-chip is then inserted between the mirrors of the Fabry-Pérot cavity. **(c)** It is possible to convert a signal (green) from microwave to optical frequencies and vice-versa by having the microwave cavity pumped with light red-detuned from its resonance by  $\Delta_e$  and the optical cavity pumped with light red-detuned by  $\Delta_o$ . (Image credit: Andrews et al. [5])



### 2.3.3 Magnetic Resonance Force Detection using SiN Membranes

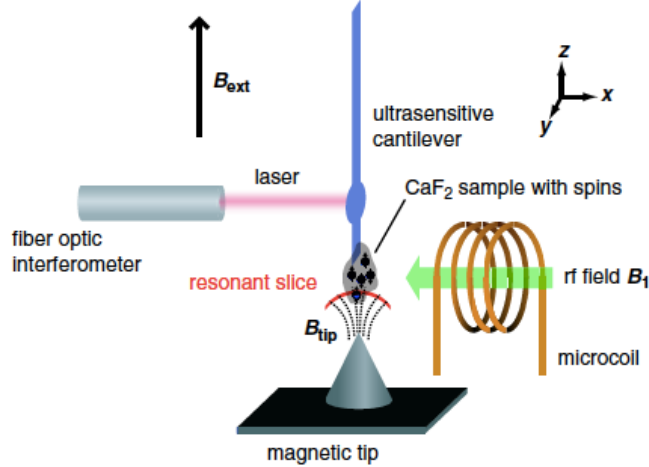
As a final experiment using SiN membranes, let's consider its use in measuring magnetic resonances. Traditionally, spin in a material are excited by an external oscillating magnetic field, which causes them to precess and transition between states, which can then be detected by a coil or microwave cavity [9, 30]. Such techniques, however, are limited in detecting ensembles with at least  $10^{12}$  nuclear and  $10^8$  electron spins [28]. Stronger coupling between the detecting device and the spins are required if sensitivity is to be increased, and one proposal is to detect the spins by using a mechanical oscillator [28, 29]

Magnetic resonance force microscopy (MRFM) uses a mechanical oscillator to detect the oscillating forces induced by the modulation of the magnetization of the spin sample by the external oscillating field. Clearly, if the resonant frequencies of the oscillator is appropriately chosen, its amplitude, dependent on the force due to the spins, may be measured via optical interferometry. More specifically (Fig. 2.6), Let's consider a cantilever as the mechanical oscillator. We can either attach the spin sample to it or the magnet that will provide the magnetic gradient. Affected by the this gradient and an external rf signal, spins previously excited by an external field will create an oscillating force felt by the cantilever, which will respond accordingly. Finally, its position can then be detected by the by reflecting light off of it. This approach has been successfully used in measuring an individual electron spin, a contrasting result compared to the more traditional approach [30].

Cantilevers used in MRFM have shown an incredible force sensitivity of  $0.82\text{aN}/\sqrt{\text{Hz}}$ , which means they can sense, “in less than a second, a force as small as the gravitational attraction between a person in Los Angeles and another in New York [2].” Nonetheless, the cantilevers have a few limitations: they are very fragile, making it difficult to deposit samples or magnets on them, they can twist and bend out-of-mode, which generates noise at the interferometer, and their characteristic frequencies are not high enough for detecting nuclear spins [19]. Therefore, the Hammel group at Ohio State University has elaborated a MRFM experiment that uses low stress

silicon nitride membranes as the mechanical oscillator.

Figure 2.6: A schematic representation of an MRFM experiment done by Degen et al. [28]. In order to detect the spins from a  $\text{CaF}_2$  sample, the group attached it to a cantilever which is positioned along an external  $B_{\text{ext}}$  field and close to the magnetic gradient of a magnetic tip. An RF coil is then responsible for exciting the spins in the sample, creating an oscillatory force that moves the cantilever, which can be precisely detected with an interferometer. (Image credit: Degen et al. [28])

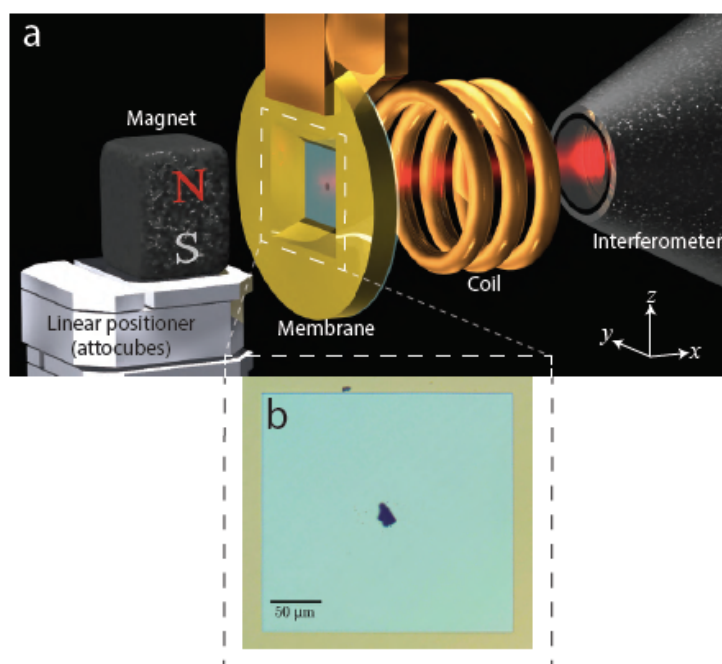


The SiN membranes address all the shortcomings of using a cantilever as the mechanical oscillator in MRFM. First, their planar dimension and clamped boundaries make it easier to deposit samples and read out their mode shape. Second, they can have several easily accessible modes at MHz frequencies, which increases their magnetic resonance measuring scope [19]. Despite its benefits and practicality, the force sensitivity of the SiN is about an order of magnitude larger than that for a cantilever,  $8\text{aN}/\sqrt{\text{Hz}}$ .

Intuitively, the limit on the force sensitivity of a mechanical resonator is reached when its motion due to thermal fluctuation is larger than that due to an external force. Thus, the force sensitivity will depend on the resonator's quality factor, since higher Qs result in better thermal decoupling (eq. 2.5), and on the thermal bath temperature. In fact, the expression for the thermal force noise [19] is

$$S_f^{1/2} = \left( \frac{2kk_bT}{\pi Qf} \right)^{1/2} \quad (2.6)$$

Figure 2.7: **(a)** A representation of the Hammel's group MRFM experiment using a SiN membrane. Here, the spin sample is attached to the membrane, which is held between the RF coil and the magnet, which itself can be positioned using attocubes. An optical interferometer measured the membrane's displacement due to the force induced by the spins of the sample. **(b)** An image of the SiN with the deposited sample. (Image credit: Scozzaro et al. [19])



where  $k$  is the spring constant of the resonator,  $k_b T$  its mean thermal energy, and  $Qf$  relates to its how decoupled it is from thermal decoherence, again according to eq. 2.5.

An equivalent expression, emphasizing different parameters of the resonator [17], is

$$S_f = \left( \frac{8m_{\text{eff}}k_b T}{\tau} \right)^{1/2} = x_{\text{zpf}} \sqrt{\frac{\hbar k_b T}{Q}} \quad (2.7)$$

where  $m_{\text{eff}}$  is the effective mass of the resonator, and  $\tau$  is the ringdown time. Both are defined respectively, as follows: consider a mode of a oscillator composed of  $x(t)$ , the amplitude of the mode, and  $u(\vec{r})$ , the a-dimensional shape of the mode. The equation of motion of  $x(t)$  will be given by the a harmonic oscillator equation for the effective mass  $m_{\text{eff}}$  [22]. Now, consider the resonator oscillating with amplitude  $x(t)$  at a resonance. After the external drive is stopped, it will continue to oscillate, with an exponentially decreasing  $x(t)$ , for a characteristic time  $\tau$ , the ringdown time. In fact, measurement of quality factors is done precisely by exciting a resonator's mode, then cutting off the driving force and measuring the amplitude ringdown. The exponential fit to this data will give the ringdown time, to which Q is inversely proportional.

## Chapter 3

### Loss mechanisms for Silicon Nitride

#### 3.1 Introduction

A common theme of the experimental applications in the previous section is that larger quality factors, i.e., lower dissipation  $\Gamma_M$ , is always beneficial. Therefore, in designing low loss systems, one needs to address the different loss mechanisms, which have been classified into two categories:

- **Internal Losses** caused by anharmonic effects, such as out-of-phase oscillating stress and strain, and relaxation of material defects [12, 13, 14].
- **External Losses** caused by lossy interactions with the surroundings, such as losses induced by surrounding air, or elastic waves transferring energy from the resonator into the substrate [22].

These dissipation mechanisms are independent of each other, in such a way that the quality factor of a mechanical oscillator can be separated into internal- and external-loss determined portions

$$\Gamma_{tot} \propto \frac{1}{Q_{tot}} = \frac{1}{Q_{internal}} + \frac{1}{Q_{external}} \quad (3.1)$$

In the following, we briefly discuss how these losses occur in SiN resonators, and how they can be addressed.

### 3.1.1 Internal Losses

Let's initially consider one of the characteristic modes of oscillation of a silicon nitride string with mode-shape (as discussed by Unterreithmeier et al [12]). The resulting displacement, given by  $z(x, t) = u(x)a(t)$ , of the string is periodic, but we are only concerned with the time independent mode-shape given by  $u(x)$ . The change of the string to  $u(x)$  from a flat, non-excited initial shape  $z(x, 0) = 0$  necessarily results in a strain distribution, given by  $\epsilon(x, z, t) = \epsilon(x, y)e^{(i2\pi ft)}$ . The displacement of the beam will likewise make the initial stress  $\sigma_0$  of a prestressed beam oscillate  $\sigma(x, z, t) = \sigma(x, y)e^{(i2\pi ft)}$  out of phase with the stress, which induces an imaginary Young's modulus  $E = \sigma/\epsilon = E_1 + iE_2$  that relates stress and strain as follows

$$\sigma(x, z) = (E_1 + iE_2)\epsilon(x, z) \quad (3.2)$$

The imaginary part of the Young's modulus is related to the mechanical dissipation of the string, which can be expressed as

$$\Delta U = \delta V \pi E_2 \epsilon^2 \quad (3.3)$$

Where  $\delta V$  is volume element of the string, which can be integrated to obtain the total loss

$$\Delta U_{tot} = \pi E_2 \int dV \epsilon^2 \quad (3.4)$$

According to the supplementary information to Unterreithmeier et al. [12], the total dissipation given by eq. 3.4 can be divided between the strain caused by elongation of the string and by its bending, with the contribution from bending being much larger than that from elongation. In fact, considering the bending energy being entirely due to the losses is an appropriate approximation [12].

The total energy in the SiN string can also be considered the as being composed of elongation and bending contributions:

$$\delta U_{tot} = \delta Q_{\text{elongation}} + \delta U_{\text{bending}} = \delta V \left( \underbrace{\sigma_0 \epsilon}_{\text{elongation}} + \underbrace{\frac{1}{2} E_1 \epsilon^2}_{\text{bending}} \right) \quad (3.5)$$

The dissipation rate  $\Gamma$  of the string will can then be expressed as

$$\Gamma \approx \frac{\Delta U_{\text{bending}}}{U_{\text{bending}} + U_{\text{elongation}}} \quad (3.6)$$

By eq. 3.5, the elongation energy  $U_{\text{elongation}}$  increases linearly with initial stress  $\sigma_0$ , but it does not affect the bending energy nearly as much, nor the dissipation associated with it. Therefore, an strategy in decreasing dissipation is to have a resonator made of high-stress material [12] (Fig. 3.1). In fact, the more energy there is in elongation, and the higher the stress, the lower the dissipation. If  $\sigma_0$  is high enough, this quality factor improvement from the elongation can be expressed as [13]

$$Q_{\text{string}} = \frac{U_{\text{elongation}}}{U_{\text{bending}}} Q_{\text{bending}} \quad (3.7)$$

Eq. 3.8 can be further improved by taking into account that  $u(x)$  is not perfectly sinusoidal, since near the clamping to the substrate it bends as a rigid cantilever being pushed at the free-standing side (Fig. 3.2). Schmid et al. have considered the effects of the cantilever-like displacement of the string into its quality factor

$$Q_{\text{string}} = \left( \frac{U_{\text{String-bending}}}{U_{\text{elongation}}} + \frac{2U_{\text{cantilever-bending}}}{U_{\text{elongation}}} \right)^{-1} Q_{\text{bending}} \quad (3.8)$$

$$= \left( \frac{(n\pi)^2}{12} \frac{E}{\sigma_0} \left( \frac{h}{L} \right)^2 + 1.0887 \sqrt{\frac{E}{\sigma_0} \frac{h}{L}} \right)^{-1} Q_{\text{bending}} \quad (3.9)$$

where  $n$  is the mode number,  $E$  is the Young's modulus,  $h$  is the the string thickness, and  $L$  its length. Because  $h/L < 1$  and  $E/\sigma_0 < 1$ , the bending at the clamp, where  $u(x)$  is cantilever-like, is the one the contributes the most to the mechanical loss.

For a silicon nitride membrane the internal loss analysis is the same. The oscillation of the membrane induces oscillating strains and stresses that dissipate energy because they oscillate out-of-phase. Generalizing eq. 3.4 to two dimensions and substituting for the strain [14] results in

$$\Delta U_{\text{mem}} = \int z^2 dz \int \int \frac{\pi E_2}{1 - \nu^2} \left( \underbrace{\left( \frac{\partial^2 u}{\partial x^2} + \frac{\partial^2 u}{\partial y^2} \right)}_{\text{mean curvature}} + \underbrace{\dots}_{\text{other terms}} \right)^2 dx dy \quad (3.10)$$

Which can be compared to the total stored energy to give the quality factor of the membrane:

$$U_{\text{mem}} = \frac{\rho h \omega^2}{2} \int \int u(x, y)^2 dx dy \quad (3.11)$$

Figure 3.1: (a) Energy stored in elongation and bending as a function of stress for a SiN string. The elongation energy increases linearly with stress, and after a high enough stress it dominates the total energy. (b) As stress is increased, together with the fraction of the total energy from elongation energy,  $Q$  increases, as expected. (Image credit: Unterreithmeier et al. [12])

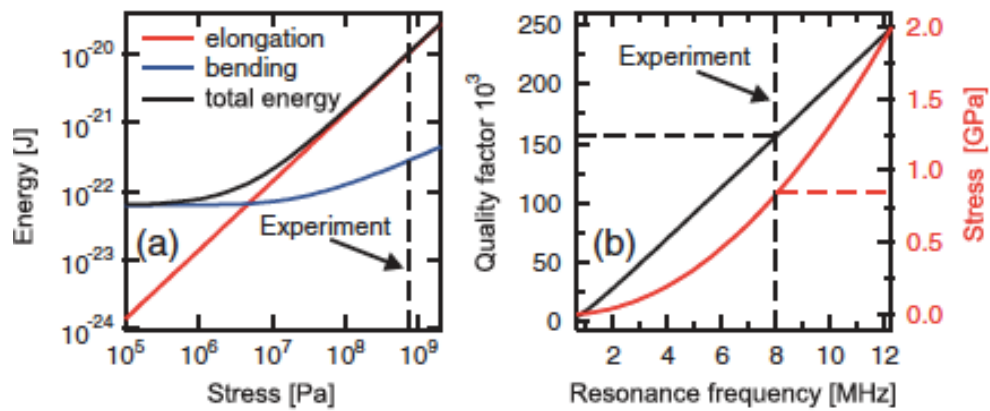
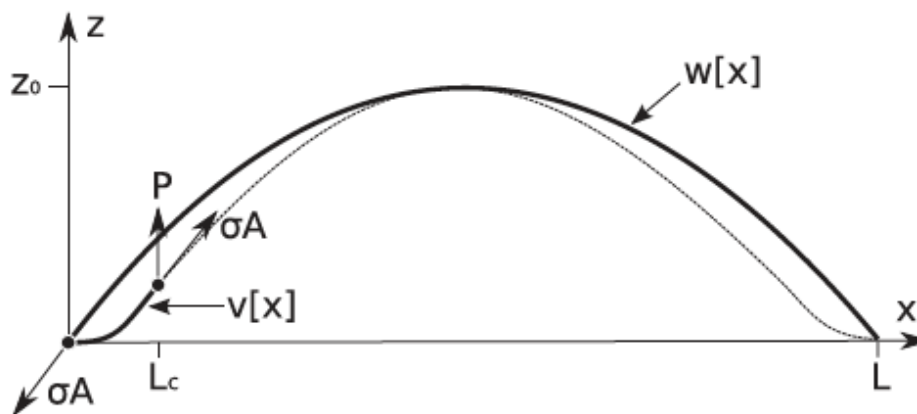


Figure 3.2: The mode shape  $u(x)$  of a SiN string is not a perfect sinusoidal like  $w(x)$ . Out from the clamping edge to a distance  $L_c$ , the string bends up like a cantilever under a tension force  $\sigma A$ ,  $\sigma$  being the intrinsic SiN stress and  $A$  the cross-sectional area of the string. (Image credit: Schmid et al. [13])



$$Q = 2\pi \frac{U_{\text{mem}}}{\Delta U_{\text{mem}}} \quad (3.12)$$

where, in eq. 3.10  $\rho$  is the membrane’s mass density,  $h$  the membrane thickness, and  $\omega$  the mode’s frequency.

In summary, by taking into account only the internal losses, the quality factor  $Q$  is determined by the bending, or curvature, of the resonator’s mode. For  $\text{Si}_3\text{N}_4$ , the high 1GPa stress increases the energy stored in the elongation of modes (besides increasing the mode frequencies), which increases their  $Q$  by eq. 3.8. Therefore, by increasing the resonator’s stress and decreasing the bending at the clamping edges, internal loss can be greatly attenuated.

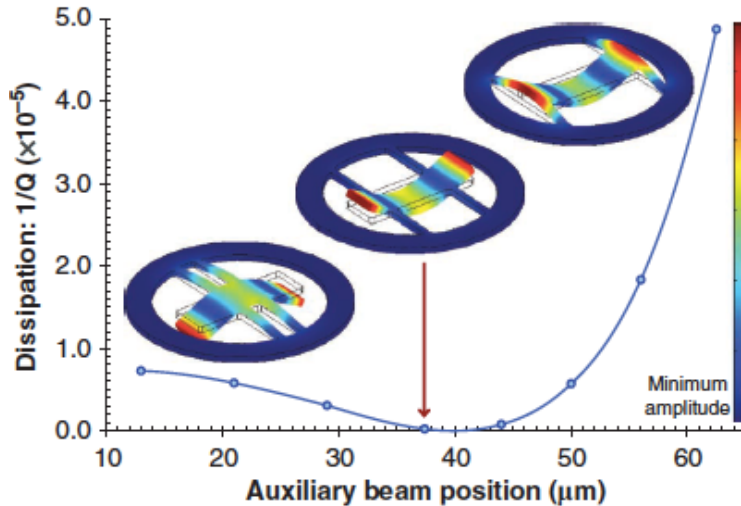
### 3.1.2 External Losses

The clamping edge of SiN mechanical resonators also takes a prominent role in determining external losses. In an intuitive sense, if the mode of the resonator *extends* to its substrate, part of its total energy will radiate out to the surrounding, at a rate dependent on the substrate’s dissipation. In any realistic experiment, the substrate will be considerably lossier than the resonator, and its “mode-extension” to the substrate will create considerable loss. More fundamentally, phonons carrying mechanical energy, i.e., quanta of elastic waves, can leak from the resonator to the substrate, causing the resonator to dissipate its energy into the environment. In reality, the theory behind these phonon leakage is much more complicated and, for the purpose of this thesis, the phonon-tunneling theory developed by Wilson-Rae [10] will be condensed to its practical applications in designing mechanical resonators of high  $Q_{\text{external}}$ , following the results of Cole et al. [11].

The coupling of resonator and substrate modes that causes leakage of vibrational energy is strongly geometry dependent. Specifically, the two biggest contributors to the external loss are the cross-sectional size and the magnitude of the displacement of the contact between the resonator and the substrate [11, 31]. Intuitively, resonators clamped by small, relatively stationary “edges” will induce less vibration and bending of the substrate, which will dissipate less of the resonator’s energy. Cole et al. [11] have confirmed this fact experimentally by simulating and measuring the dissipation of the same mechanical mode connected to a substrate through different geometries.

Similar simulations were done by [31], where they observed  $Q$ s three times higher for geometries where the connection was made to a node of the resonator mode.

Figure 3.3: Cole et al. simulation results of the influence of the location of the connecting beam between resonator and substrate. For the same resonator mode, whenever the connecting beam moves the least with the resonator is the one that dissipates the least, since it is also the when induced motion at the substrate is the smallest, which implies less energy will be leaked out. (Image credit: Cole et al. [11])



### 3.2 Loss-Attenuating Designs

A better understanding of the loss mechanisms as discussed in the previous section have inspired new designs for  $\text{Si}_3\text{N}_4$  membrane resonators. The first approach discussed below, the **Phononic Crystals (PnC)** designs, consists of patterning the substrate to which the membrane is attached such that no elastic waves from membrane modes can propagate across it and leak elastic energy. Despite addressing only external loss, the phononic crystals were able to increase the quality factors of high-stress silicon nitride membranes by two orders of magnitude.

Another approach is a tethered-membrane design called a **Trampoline**. Here, a square  $\text{Si}_3\text{N}_4$  square membrane is suspended from the substrate by 4 string like  $\text{Si}_3\text{N}_4$  tethers. The original, uniform high stress of the  $\text{Si}_3\text{N}_4$  redistributes, concentrating on the tethers and diminishing considerably in the connection of the tethers with the substrate, which greatly decreases the internal

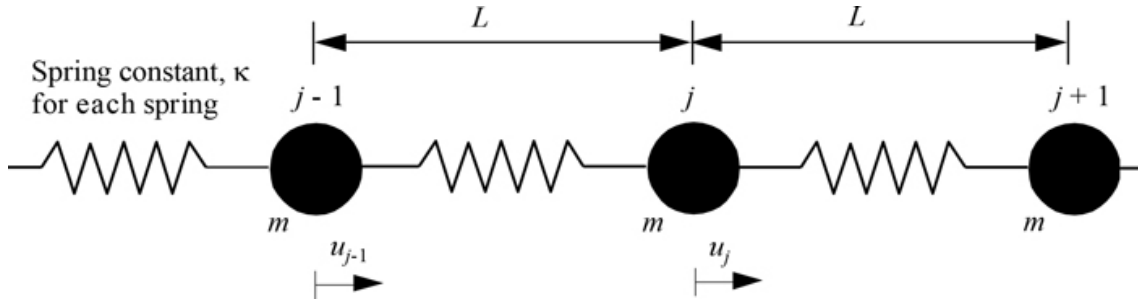
losses. Moreover, by having smaller connections to the substrate, one expects the external losses are also decreased in this design.

Finally, another design is to pattern a PnC with a central defect directly onto a  $\text{Si}_3\text{N}_4$  membrane. This approach combines the PnC decoupling of resonator and substrate and the decrease of bending at the clamping edges, since the modes decay exponentially in the  $\text{Si}_3\text{N}_4$  PnC before getting to the edges. The measured quality factors of this design has also shown a considerable improvement compared to pure membranes, as is discussed below.

### 3.2.1 Silicon Substrate PnC: Theory and Experiment

In order to understand the phononic crystal design, let's first start with a 1D chain of identical point masses of mass  $m$  connected by springs of constant  $\kappa$ , which follows closely chapter 10 of Simons textbook [32]. If the distance between each of the masses to be  $L$ , the potential energy of the system will be

Figure 3.4: A 1D chain of equal masses connected by springs. The distance between each mass, also called the *lattice constant*, is  $L$ , and the displacement of each mass from its equilibrium position is  $u$ . (Image credit: Levi, *Essential Classical Mechanics for Device Physics*. (2016)



$$V_{tot} = \sum_j V(x_{j+1} - x_j) = \sum_j \frac{\kappa}{2} (x_{j+1} - x_j - a)^2 = \sum_j \frac{\kappa}{2} (u_{j+1} - u_j)^2 \quad (3.13)$$

where  $u_j = x_j - jL$  is the displacement of the  $j^{\text{th}}$  mass from its equilibrium position  $x_{j,eq} = jL$ .

The force  $F_n$  of the  $n^{\text{th}}$  mass can be found by differentiating eq. 3.13 with respect to  $x$ :

$$F_n = -\frac{\partial V_{tot}}{\partial u_n} = \kappa(u_{n+1} + \delta x_n) + \kappa(u_{n-1} - u_n) \quad (3.14)$$

From which we can find the equation of motion for each mass

$$m(\ddot{u}_n) = F_n = \kappa(u_{n+1} - 2u_n + u_{n-1}) \quad (3.15)$$

Now we use the wave ansatz  $u_n = Ae^{i\omega t - ikx_{n,eq}} = Ae^{i\omega t - iknL}$  in eq. 3.15, obtaining

$$-m\omega^2 Ae^{i\omega t - iknL} = \kappa Ae^{i\omega t} (e^{-ik(n+1)L} - 2e^{-iknL} + e^{-ik(n-1)L}) \quad (3.16)$$

$$m\omega^2 = 2\kappa(1 - \cos(kL)) = 4\kappa\sin^2(kL/2) \quad (3.17)$$

$$\omega = 2\sqrt{\frac{\kappa}{m}} \left| \sin\left(\frac{kL}{2}\right) \right| \quad (3.18)$$

The relation between frequency  $\omega$  and wavevector  $k$  is known as the **dispersion relation** of the system, which is clearly periodic with period  $k \rightarrow k + 2\pi/L$ . In fact, if the system has a length period of  $L$ , its *reciprocal lattice* over  $k$ -space will be periodic with period  $2\pi/L$ , with the periodicity unit that repeats itself over  $k$ -space known as its *Brillouin zone*. Figure 3.5 shows the dispersion relation for eq. 3.18 marked as 1, which indicates the maximum frequency the system can assume,  $\omega_{\max} = 2\omega_0 = 2\sqrt{\kappa/m}$ .

Let's now consider a 1D chain where the spring constant values alternate between  $\kappa_1$  and  $\kappa_2$ , that is, in Fig. 3.4 the spring between points  $j - 1$  and  $j$  will have constant  $\kappa_1$  and the spring between  $j$  and  $j + 1$  will have constant  $\kappa_2$ . Because two adjacent masses will have a different spring order attached to them, their displacement will then be  $x_n$  and  $y_n$  (see Fig. 3.6) and the lattice constant  $L$  will include two masses, forming the *unit cell* of the lattice.

Using the approach above for each coordinate  $x_n$  and  $y_n$ , the dispersion relation for the diatomic chain of Fig. 3.6 will have two branches [32], one for each degree of freedom of the unit cell

$$\omega_{\pm} = \sqrt{\frac{\kappa_1 + \kappa_2}{m} \pm \frac{1}{m} \sqrt{(\kappa_1 + \kappa_2)^2 - 4\kappa_1\kappa_2\sin^2(ka/2)}} \quad (3.19)$$

Figure 3.5: A 1D chain of equal masses connected by springs. The distance between each mass, also called the *lattice constant*, is  $L$ , and the displacement of each mass from its equilibrium position is  $u$ . (Image credit: Levi, *Essential Classical Mechanics for Device Physics*. (2016))

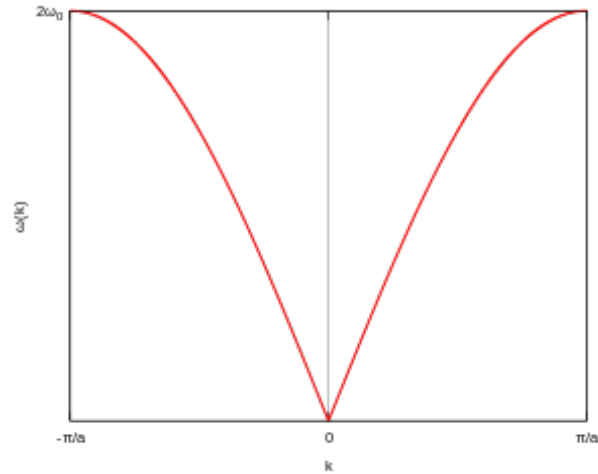
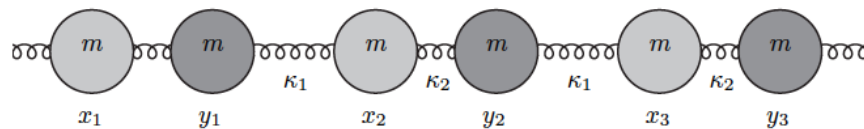
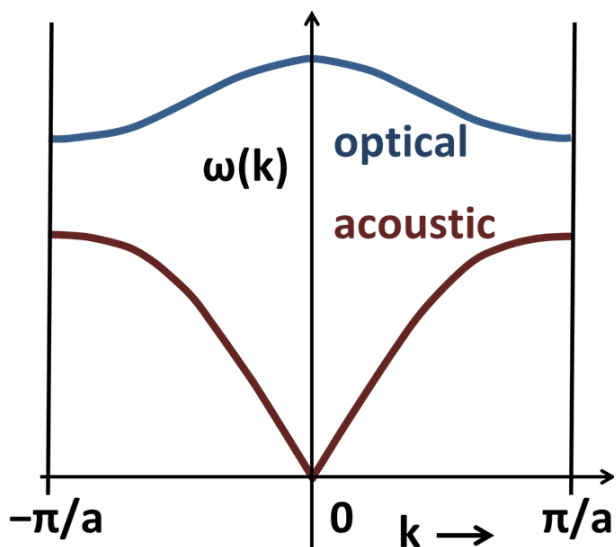


Figure 3.6: Now we consider a chain with two values for spring constants  $\kappa_1$  and  $\kappa_2$ . Because two adjacent masses will be connected different to the springs, their displacement will be different, denoted  $x_n$  and  $y_n$ . Finally, because the periodicity unit has to include both masses, which then repeat along the system. This unit is called the *unit cell*, which spans the system when repeated over the lattice points. (Image credit: Simon [32])



which results in the the plot of Fig. 3.7. The lower-energy, larger wavelength branch  $w_-$  corresponds to acoustic waves in which the unit cell moves in unison, which is similar to the dispersion relation in Fig. 3.5, and the higher energy optical branch  $w_+$ , corresponds to out-of-phase oscillations of the two atoms in a cell. These are called optical because they can interact with incident photons, a theme explored more in chapter 5.

Figure 3.7: The dispersion relation for a unidimensional chain with two different masses or springs. The dispersion relation will be divided into two branches (one for each degree of freedom of the system). The low frequency, large wavelength corresponds to acoustic normal modes, whereas the high energy correspond to optical modes that can interact with incident photons. (Image credit: wikipedia.org).



Notice that the acoustic and optical branches never intersect, making a **band-gap** of “forbidden” values for  $\omega(k)$ . This happens because  $\kappa_1 \neq \kappa_2$ , since the maximum value the acoustic branch  $\omega_-(\pm\pi/L) = \sqrt{2\kappa_1/m}$  is smaller than the minimum value of the optical branch  $\omega_+(\pm\pi/L) = \sqrt{2\kappa_2/m}$ . The band would close if  $\kappa_1 = \kappa_2$ , and the shape of the dispersion relation would be the same as in Fig. 3.5, but with double the size. In other words, the **reciprocal unit cell** (reciprocal because  $[k] = 1/\text{distance}$ ) would be twice as big in this case because the unit cell would include two masses and would also be twice as big. Consequently, as the difference between  $\kappa_1$  and  $\kappa_2$  is increased, the largest the band-gap between them will become, moving the

two branches farther apart. The split of the two branches and the formation of a band-gap would also happen if instead of different elastic constants we had different masses in the unit cell, since  $\omega_{-}(\pm\pi/L) = \sqrt{2\kappa/m_1} \neq \sqrt{2\kappa/m_2} = \omega_{+}(\pm\pi/L)$ .

For 2D structures, the dispersion relation will also be given as  $w(k)$  over all values of  $k$  in the reciprocal unit cell, the only difference being how complicated the reciprocal unit cell in this case is (for more details, see chapters 12 and 13 of [32]). As in the case of a 1D chain, if a 2D unit cell contains regions of different mass or spring constant, a band-gap can open up in the dispersion relation, preventing normal modes with certain frequencies. Thus, if such a 2D structure is the substrate to a  $\text{Si}_3\text{N}_4$  membrane, normal modes of the membrane with frequencies in the band-gap won't be able to extend to the substrate and induce any motion, diminishing external loss.

Yu et al. [15] have successfully applied the idea of patterned substrate with a band-gap to isolate membrane modes and significantly decrease energy leakage. The commercially available 1cm-across silicon chip with a 0.5mm  $\text{Si}_3\text{N}_4$  membrane was patterned into a PnC crystal composed of a mesh of high-mass squares connected by low-mass tethers (Fig. 3.8(a)). The central high-mass square encloses the membrane, whose normal modes inside the PnC crystal band-gap should not excite neither its immediate frame, nor the surrounding (according to the colored points in Fig. 3.8(b)), but if a membrane mode is outside the crystal's band-gap, then the mode and its energy should leak out. The band-gap of the PnC crystal can be plotted by tracing the dispersion relation for the reciprocal unit cell vectors as indicated in Fig. 3.8(c). the wavevector  $\vec{k}$  goes from the reciprocal space origin denoted  $\Gamma$ , goes to  $X$ , follows to  $M$ , and then returns to  $\Gamma$ . The resulting frequency response  $\omega(k)$ , depicted in Fig. 3.9, clearly indicates two band-gap regions, one centered around 3MHz and another just under 4MHz.

The decoupling of membrane and crystal modes was measured using Mach-Zehnder interferometry (see Fig. 3.10(a) for a in-band-gap membrane mode, and Fig. 3.10(b) for a out-band-gap membrane mode). At mK temperatures, these PnC crystal chips have allowed quality factors more than an order of magnitude higher than those for un-patterned chips.

Figure 3.8: **(a)** The Si PnC crystal (blue) surrounding the membrane (yellow). **(b)** Membrane, membrane frame, and adjacent large-mass square in the PnC. If a membrane mode is within the band-gap of the PnC, only the membrane should oscillate, but not the surrounding PnC. **(c)** Unit cell of the PnC crystal and the reciprocal cell vectors. The dispersion relation for this structure is obtained by tracing  $k$  along the vectors and plotting  $\omega k$ . (Image credit: Yu et al. [15]).

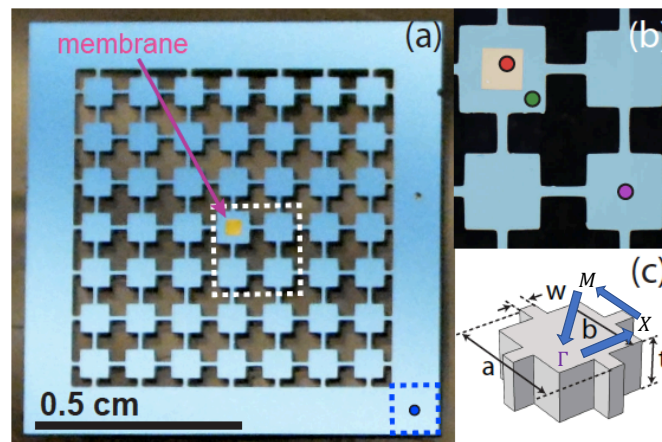


Figure 3.9: The dispersion relation for the unit cell depicted in Fig. 3.8(c). Again,  $k$  spans three different directions, first along the vector connecting the reciprocal lattice points  $\Gamma$  and  $X$ , then  $X$  and  $M$ , and finally  $M$  and  $\Gamma$ . The corresponding dispersion relation shows two band-gaps, one around 3MHz and another just below 4MHz (Image credit: Yu et al. [15]).

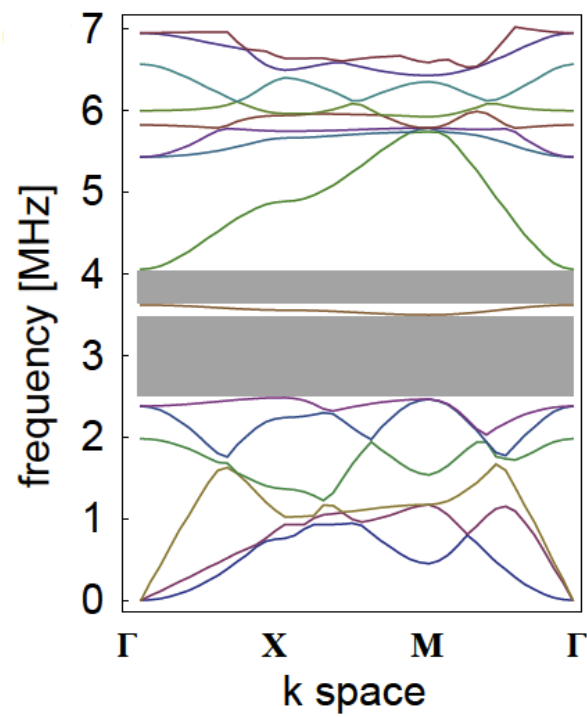
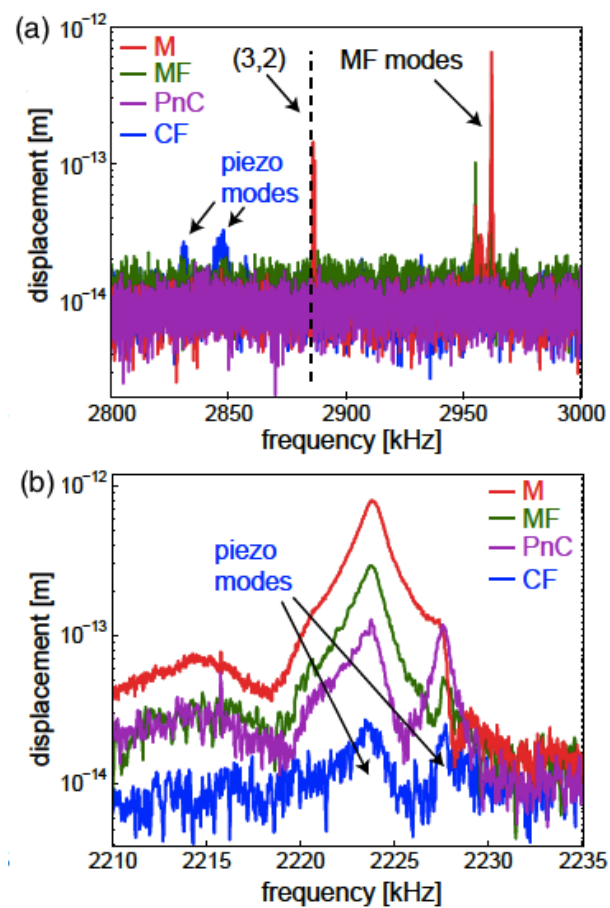


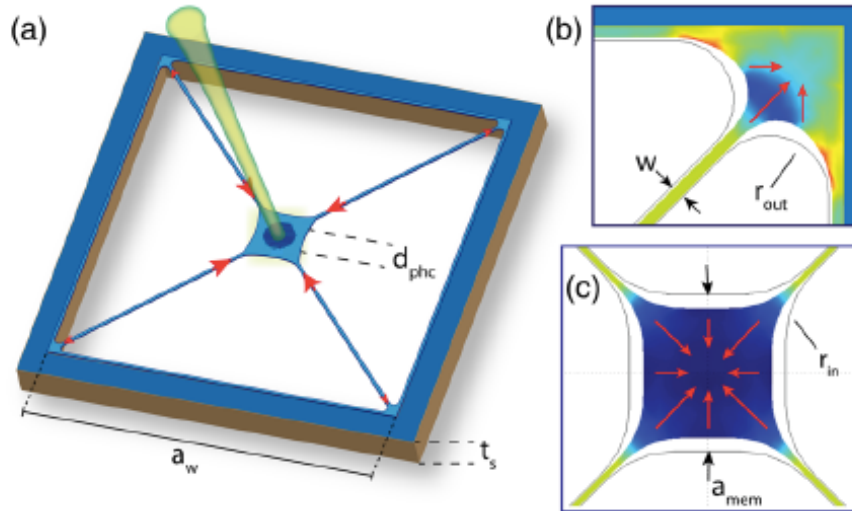
Figure 3.10: **(a)** Displacement of different parts of the system for in-band-gap frequencies, according to Fig. 3.8(b). Notice that only the membrane and its immediate frame actually move for membrane modes. The PnC and the chip frame remain stationary, except for some piezo modes excitation. **(b)** Out-of-band-gap displacements. Here, all parts of the system have a resonant mode around 2224kHz, which indicates the membrane modes are coupled to the substrate, which, as seen above, will cause energy to dissipate (Image credit: Yu et al. [15]).



### 3.2.2 An Overview of Trampolines

Another design that addresses both external and internal losses is the trampoline, which is obtained by patterning the  $\text{Si}_3\text{N}_4$  membrane into a smaller membrane region connected to the substrate by tethers. The uniform, high initial stress  $\sigma_0$  of the membrane is reduced in the tether membrane connection, increasing tether elongation (blue colors on Fig. 3.11(c)). Additionally, for sufficiently large outer fillet radius  $r_{\text{out}}$ , the bending close to the clamping edges will be greatly reduced, as the high stress holds the “flaps” in place.

Figure 3.11: (a) Overall geometry of a  $\text{Si}_3\text{N}_4$  trampoline. (b) and (c) The new geometry redistribute the initial stress of the membrane, providing elongation of the tethers and reducing the bending at the clamping edges, which are obviously also reduced in size (Image credit: Norte et al. [16]).



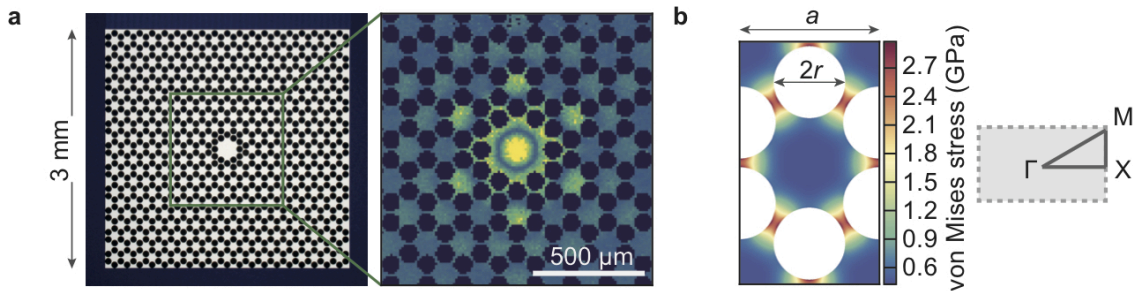
Norte et al. have measured an incredibly high room temperature quality factor of  $10^8$ , which was obtained by optimizing the parameters shown in Fig. 3.11: tether width  $w$ , central membrane size  $a_{\text{mem}}$ , window size  $a_w$ , and outer and inner fillet radii  $r_{\text{in}}$  and  $r_{\text{out}}$ . Most changes in these parameters change the quality factor  $Q$  and mode frequency  $f$  in such a way that the  $fQ$  product remains the same; the exception being membrane size  $a_{\text{mem}}$ , which when increased decreases the  $fQ$  product, and outer fillet radius  $r_{\text{out}}$ , which when increased also increases the  $fQ$  product [16].

### 3.2.3 Silicon Nitride PnC with Membrane-like Defect

A final design that addresses the loss mechanisms in silicon nitride is the  $\text{Si}_3\text{N}_4$  PnC with a central defect (Fig. 3.12(a)), which combines the decreased external loss of a PnC with less bending of the resonator near the clamping edges, which decreases the internal losses. This design manages to decouple the modes of the central defect from those of the surrounding PnC without an abrupt change of the mode at the edge of the defect and PnC. In fact, the defect's mode decays exponentially along the PnC region, eliminating the “extreme bending” of the membrane at the edge with the substrate (i.e, of the defect with the crystal, and then of the crystal with the Si substrate).

Because the nearly 2D unit cell in this design is made of  $\text{Si}_3\text{N}_4$ , the initial uniform stress distribution changes, increasing at the cell tethers and decreasing at the central pad (Fig. 3.12(b)). The unit cell lattice constant  $a$  control for all other elements of the cell, more importantly the radius of the “wholes” in the crystal.

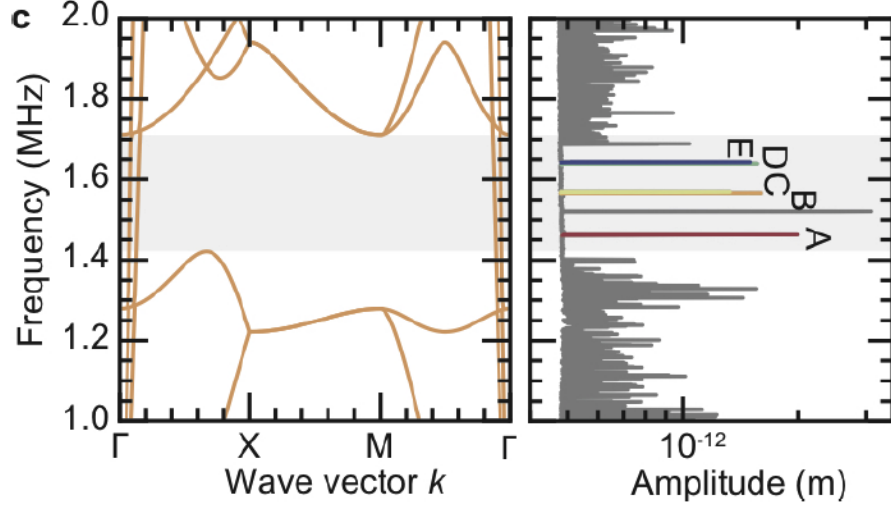
Figure 3.12: **(a)** Geometry of the  $\text{Si}_3\text{N}_4$  phononic crystal designed by Tsaturyan et al. [18]. The regular lattice pattern is broken at the very center by a membrane like defect, whose in band-gap mode is depicted. Notice how the mode amplitude decreases more “softly” across the PnC, which allows for less curvature overall and reduced internal loss. **(b)** The hexagonally symmetric unit cell shows a stress redistribution similar to that of a trampoline (Fig. 3.11(b)) (Image credit: Tsaturyan et al. [18]).



The dispersion relation following the path in the reciprocal lattice shown in fig. 3.12(b) leads to a band-gap 300Hz wide around 1.5MHz which includes five defect modes, all measured having much greater amplitude than non-defect modes of the structure within the band-gap (Fig. 3.13).

For the defect in-band-gap modes, such as mode A (Fig. 3.12(a)), the “soft clamping” of the defect to the PnC and the PnC to the results in an exponential decay of the out-of-plane motion along the crystal, as shown in Fig. 3.14.

Figure 3.13: The dispersion relation for the reciprocal cell depicted in Fig. 3.12(b) and the corresponding in band-gap defect modes (Image credit: Tsaturyan et al. [18]).

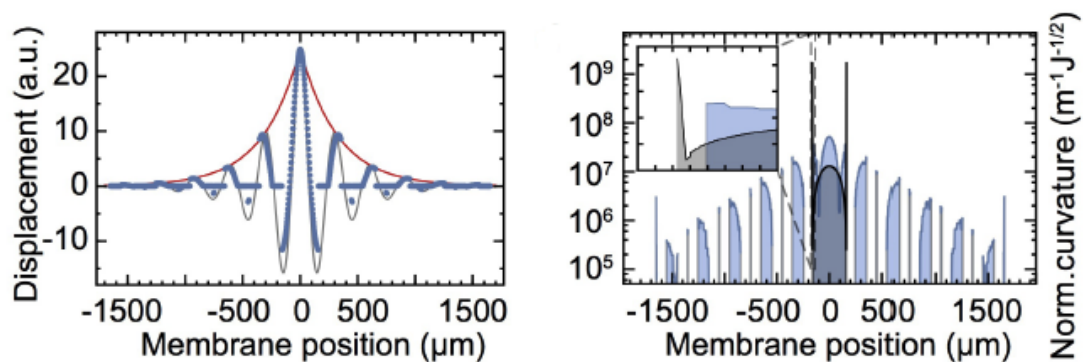


Moreover, let's consider a normalized curvature

$$\frac{\left| \frac{\partial^2 u}{\partial x^2} + \frac{\partial^2 u}{\partial y^2} \right|}{\sqrt{U_{\text{mem}}}} \quad (3.20)$$

where the numerator is the mean curvature and the denominator is the total energy of the system, given by eq. 3.11. Calculating eq. 3.20 along the  $\text{SI}_3\text{N}_4$  PnC structure and a membrane of the dimensions of the central defect reveals that, near its edges, a membrane's curvature is two orders of magnitude larger than that of the defect. Clearly, this greatly reduces the internal loss of  $\text{SI}_3\text{N}_4$  PnC, which, combined to the external loss reduction from the PnC lattice, enables a measured room-temperature  $fQ$  product  $\sim 10^{14}$ , the highest ever achieved [18].

Figure 3.14: For the first in band-gap defect mode the out-of plane, “mode-shape” displacement decays exponentially along the PnC lattice. This soft clamping corresponds to a much reduced curvature of the defect-PnC edge compared to the curvature of the membrane-substrate edge for a membrane of the same dimensions as the defect(Fig. 3.12(a)) (Image credit: Tsaturyan et al. [18]).



## Chapter 4

### FEM modeling of Hybrid Trampoline-PnC Designs

#### 4.1 Introduction

Despite the superior quality factor of trampolines due to reduced bending at the edges and, thus, less dissipation, the effects of external loss due to energy leakage are harder to understand. One of the goals of my research was to implement finite element modeling (FEM) of trampoline and substrate geometries and simulate the resulting mode coupling between the two domains. With a successful model, different trampoline geometries could be tested for their quality factor, but unfortunately the I was unable to reproduce within one order of magnitude known membrane quality factors. The first section of this chapter covers the results of these simulations.

Because modeling accurate external losses for resonators was found to ultimately be too involved, modeling low external loss  $\text{Si}_3\text{N}_4$  PnC designs proved a more successful approach. In the remaining sections of this chapter we discuss COMSOL FEM simulations of  $\text{Si}_3\text{N}_4$  PnC structures with trampoline-like defects. The motivation for including a trampoline as a defect is to have a lower mass defect-resonator, which would improve the force sensitivity of of the resonator  $S_f$ , as well as increase the optomechanical coupling  $g_0$ . This discussion is divided in two parts: (a) the correct simulation of a PnC unit cell and the calculation of the dispersion-relation and (b) the simulation of structures with finite number of cells and trampoline defects. The goal was to find a design with trampolines modes inside the bandgap of the PnC lattice, and that would be small enough (less than the 3mm sized resonators discussed in the previous chapter) for in-cavity operation. Part (a) is a reproduction of the unit cell by Tsauryan et al. [18] and a brief study of the effects of the

lattice constant  $a$  on the bandgap. Part (b) is a discussion of two models, the flower and the web, that have been found to possess trampoline modes inside the bandgap.

## 4.2 External Loss Simulation via Perfectly Matched Layers

In order to calculate and model for the quality factor of different trampoline and other  $\text{Si}_3\text{N}_4$  geometries, one can use a finite element software to numerically solve for the normal mode partial differential equations under “trampoline” geometries. In fact, only simple domains with simple boundary conditions, such as rectangles under constant-value boundaries (Dirichlet conditions), are ever solved analytically. Complex geometries with complicated boundaries and multiple external sources are usually solved via **finite elements** approach. In summary, a complex domain is partitioned into smaller subdomains where the global differential equations can be simplified to sets of algebraic equations or ODEs (for steady or transient solutions, respectively). The solutions for the subdomain equations is then recombined into a global solution for the original problem. Such an “divide-and-conquer” approach is especially suited for problems with domains with different parts, since each part can be divided into separate sets of partitions and solved separately.

The Finite element software used in this work was *COMSOL multiphysics*, which has a GUI that allows the user to draw objects, implement different physical boundary conditions, and solve numerically for multiple situations. For the results that followed, we used the structural-mechanics physics set to calculate eigenfrequencies (normal mode frequencies) and stress distributions for trampoline and PnC designs. COMSOL is also able to calculate quality factors for normal modes, if internal losses are designated to different materials used. Nonetheless, external losses need also to be included separately if COMSOL is to calculate  $Q_s$  accurately.

An usual way to implement external losses in simulations like these is to include what is called a **perfect matched layer (PML)** in the system. Such a layer is a designated subdomain that implements a coordinate transformation on incoming waves, causing the exponential decay of their amplitude before they can reflect back into non-PML subdomains [33]. Effectively, the PML is implemented as an infinite extension of a resonator’s substrate, which causes any elastic

waves to be lost inside of it. Such an approach has been successful in reproducing the measured quality factors of diamond and other resonators [34], and has become a common computational implementation of external losses [33].

We aimed to create COMSOL models that would predict the quality factor for different resonators by using PMLs for external losses. Even though bending losses would not be appropriately included, we hoped to be able to calculate Q within an order of magnitude of measured values. To make sure such models was accurate, we first used PMLs with membrane designs, since these have well known measured quality factors that we could use to validate our model.

Our model had a  $\text{Si}_3\text{N}_4$  membrane and its substrate supported from glue joints from an hemispherical invar base whose outer parts of the invar base were designated as the PML domain (Fig. 4.1). Such a model was able to reproduce satisfactorily membrane modes that clearly induced motion of the Si chip and the invar base, which showed some of the elastic waves were reaching all the to the PML as expected (Fig. 4.2).

Nonetheless, to calculate accurate quality factors with this model, it is necessary to also included the material losses for the different parts of the model, which accounts in part for the internal losses. COMSOL implements material losses using an  $\eta = Q^{-1}$  factor, which tells us that  $\eta_{\text{Si}} = 10^{-5}$  and  $\eta_{\text{Si}_3\text{N}_4} = 10^{-6}$  are good estimates. The glue we consider to be a lot lossier, however, which may contribute too much for the overall loss, as seems to be the case in Fig. 4.2, where the oscillations beying the glue joints are very reduced. Using these parameters, the calculated quality factors for the first few membrane modes (table 4.1) did not reproduce the measured behavior of considerably higher Qs for symmetric modes [14]. It is also clear that the glue joints can easily overshadowed the PML effects and, even without the the glue, the correct trend is not reproduced.

Table 4.1: Calculated Qs for membrane with PML COMSOL model.

| Glue loss $\eta_{glue}$ | 11 mode Q ( $\times 10^6$ ) | 21 mode Q ( $\times 10^6$ ) | 22 mode Q ( $\times 10^6$ ) | 31 mode Q ( $\times 10^6$ ) |
|-------------------------|-----------------------------|-----------------------------|-----------------------------|-----------------------------|
| 0 (without PML)         | 2.29                        | 21.1                        | 93.5                        | 25.6, 2.6                   |
| 0 (with PML)            | 0.0366                      | 1.28                        | 1.44                        | 0.946, 0.409                |
| 0.01                    | 0.0865                      | 1.52                        | 12.5                        | 0.980, 0.250                |
| 0.05                    | 0.0181                      | 0.320                       | 2.80                        | 0.190, 0.0490               |

Figure 4.1: Tsaturyan et al. unit cell parameters. Notice that there are only two degrees of freedom: the lattice constant  $a$  and either the size of the radius or the width of the cell tether.

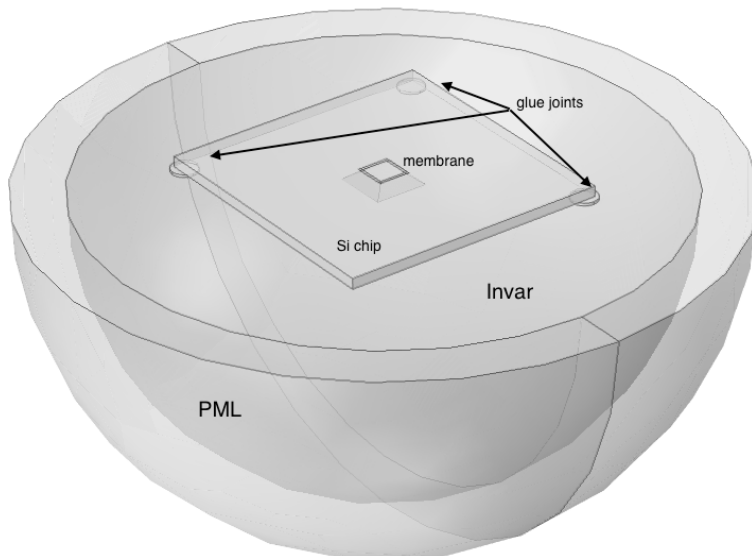
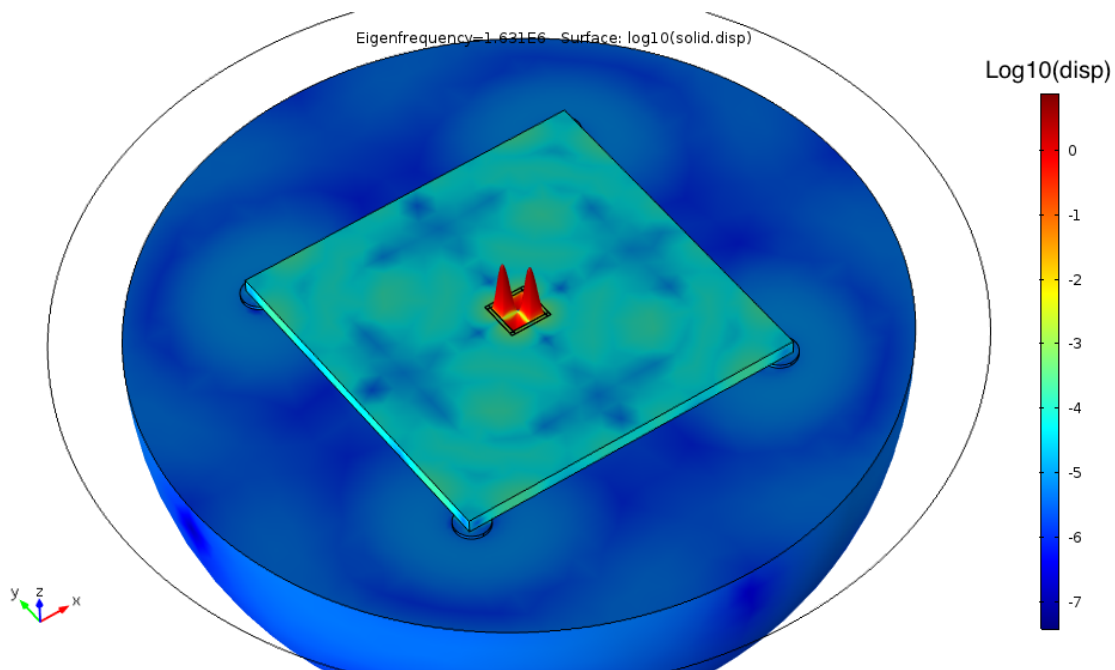


Figure 4.2: The 22 mode of a the membrane induces displacement in all parts of the geometry, which indicates external losses due to waves reaching the PML.



The fact that the glue joint affects the quality factor considerably is disheartening, because the glue amounts and shapes will never be the same from experiment to experiment. Furthermore, the fact that the glue matters so much also indicates that the PML, even if functioning correctly as a “infinite” substrate, is not enough to handle the losses of the system, and neither is it enough in conjunction with the material  $\eta$  losses of COMSOL. In fact, table 4.1 indicates that the model of Fig. 4.1 is not detailed enough, since a small factor, such as the glue which is very complicated to correctly model in a generic fashion, greatly influences the calculations results.

### 4.3 Unit Cell Simulations

Since building a model with reliable external loss parameters proved too involved, an obvious approach is to deal with a resonator design that we already know has very low external loss, such as phononic crystals. These structures can be simulated more easily, since we do not need to include in our models any exterior objects such as substrate, glue joints, etc.

#### 4.3.1 Simulation Considerations

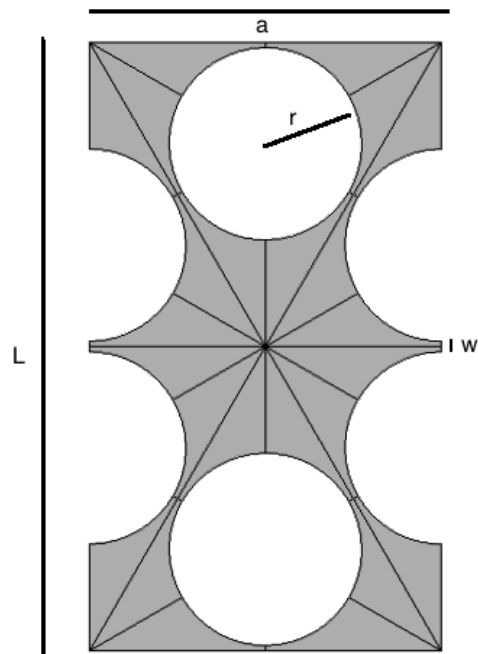
Let’s start with the geometric parameters of the unit cell by Tsaturyan et al. 3.12 (“Circular cell”). There are only two free parameters: the size of the lattice constant  $a$  and the size of the cell tether  $w$ . The long size of the cell and the radius of the holes in the cell are functions of the  $a$  and  $w$ , as shown in table 4.2 and illustrated in Fig. 4.3.

Table 4.2: Geometric parameters of Tsaturyan et al. unit cell depicted in figure 4.3.

| Parameter | Expression                           | Tsaturyan et al [18] Reference Values | Description              |
|-----------|--------------------------------------|---------------------------------------|--------------------------|
| a         | control value                        | 160 $\mu$ m                           | size of the unit cell    |
| w         | control value                        | -                                     | width of the cell tether |
| L         | $a/\sqrt{3}$                         | -                                     | long length of cell      |
| rf        | $\frac{-w}{2a} + \frac{\sqrt{3}}{6}$ | 0.26                                  | -                        |
| r         | rf $\times$ a                        | -                                     | radius of holes          |

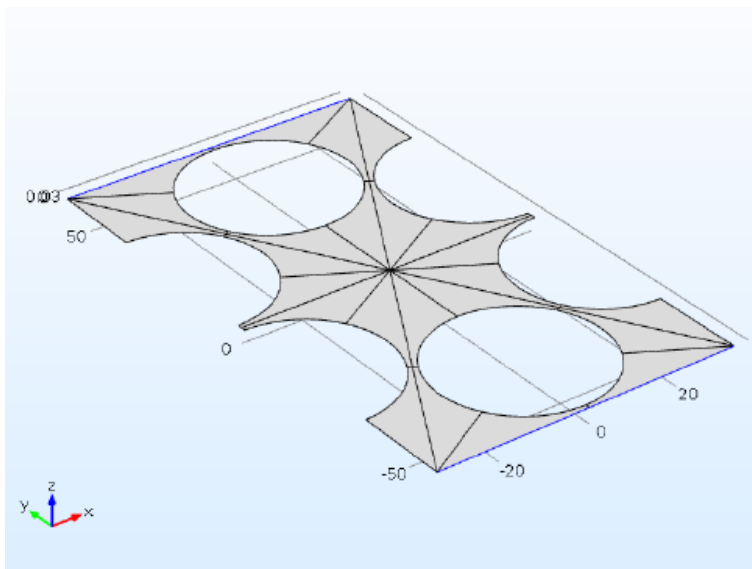
After drawing the geometry in COMSOL, the next step was to choose boundaries that demarcate the intrinsic periodicity of the PnC crystal. By choosing such boundaries, COMSOL is

Figure 4.3: Tsaturyan et al. unit cell parameters. Notice that there are only two degrees of freedom: the lattice constant  $a$  and either the size of the radius or the width of the cell tether.



capable of effectively simulating an infinite periodic structure, just like the unidimensional mass chain of Fig. 3.4, and calculate the dispersion relation for such geometry. Clearly, the very thin faces parallel to the z-axis have to be selected as the periodic boundaries. In particular, we need to use COMSOL's *Floquet Periodicity* to define wave vectors  $\vec{k}$  perpendicular and the reciprocal lattice points  $\Gamma = (0, 0)$ ,  $X = (\pi/a, 0)$ , and  $M = (\pi/a, \pi/L)$ .

Figure 4.4: One of the two sets of opposing boundaries that delimit the periodicity of the unit cell. The Floquet Periodicity indicates a periodic structure in reciprocal k-space, which is the periodicity characteristic of dispersion relation calculations, as seen in chapter 3.



In COMSOL, this takes the form of a *parametric sweep* of the coordinates of the  $\vec{k} = (kx, ky)$  in the path vector as it spans all the possible  $|k|$  values when circling  $\Gamma \rightarrow X \rightarrow M \rightarrow \Gamma$ . Table 4.3 shows how this is implemented using auxiliary values  $k1$  and  $k2$  that values from 0 to 1 in the parametric sweep.

A dispersion relation can be computed by an eigenfrequency (mode frequency), analysis for each  $(k1, k2)$  value in the parametric sweep. However, to obtain a correct result, a preliminary step is required where the stress of the cell is redistributed to match the stress of tethered-membranes as discussed in chapter 3 and shown in Fig. 3.12(b). To accomplish this in COMSOL, we must first

Table 4.3: The parameters necessary to define the basis of the k-space for the unit cell in Fig. 4.3.

| Parameter | Expression     |
|-----------|----------------|
| k1        | 1              |
| k2        | 1              |
| kx        | $(\pi/a) * k1$ |
| ky        | $(\pi/L) * k2$ |

fixate some part of the unit cell model so that the stationary (equilibrium) analysis can find a finite, singular solution (it cannot recognize that displacing the origin results in the same exact problem). However, the fixed point needs to be chosen in such a way that keeping it cannot move after the stress is redistributed. As Norte et al. trampoline indicates (Fig. 3.11(b) and 3.11(c)), everywhere in the trampoline clearly moves away from stress concentration, with the exception of the point right at the center of the membrane, since no movement would make sense if the symmetry is to be conserved under the non-uniform stress distribution. Thus, following the behavior shown by trampolines, we fixate the vertical “edge” at the center of the pads in the unit cell (Fig. 4.5). This guarantees the stationary study is capable of obtaining the correct stress (Fig. 4.6).

The eigenfrequency analysis can then use the correctly calculated stress-distribution for the unit-cell as its initial values. Effectively, COMSOL calculates all mode frequencies for the different  $\vec{k} = (k1, k2)$  values in the parametric sweep, and we can then plot them to obtain the dispersion relation (Fig. 4.7). From the figure, we can clearly see the bandgap occurs around  $1.6MHz$  and is about  $300Hz$  wide. Notice that it agrees well with the dispersion relation of Tsaturyan et al. [18] depicted in Fig. 3.13(a), despite an upward shift of  $\sim 150Hz$ . It also reproduces the lateral lines that indicate an imperfect, quasi-bandgap, due to the extreme aspect ratio of the structure. Nonetheless, this quasi-bandgap reduces external loss, as is discussed more extensively in section 4.4.

### 4.3.2 Effects of Lattice Parameter $a$ and Cell Tether size $w$

A typical dispersion relation with a bandgap as in Figs. 4.7, 3.13, and 3.9 assumes infinite periodic structures with no boundaries, as used in the derivations of section 3.2.1. Evidently, no

Figure 4.5: **(a)** Symmetry points of the unit cell that are fixed in place for the correct calculation of the stress distribution of the cell (Fig. 3.12(b)). These points were carefully chosen because, by symmetry, they will not move under a non-uniform stress-distribution, which guarantees a correct stress distribution result if they are taken as fixed. **(b)** Magnification of one of the points of Fig. 4.5. Notice that the symmetry point is actually an edge along the z-axis.

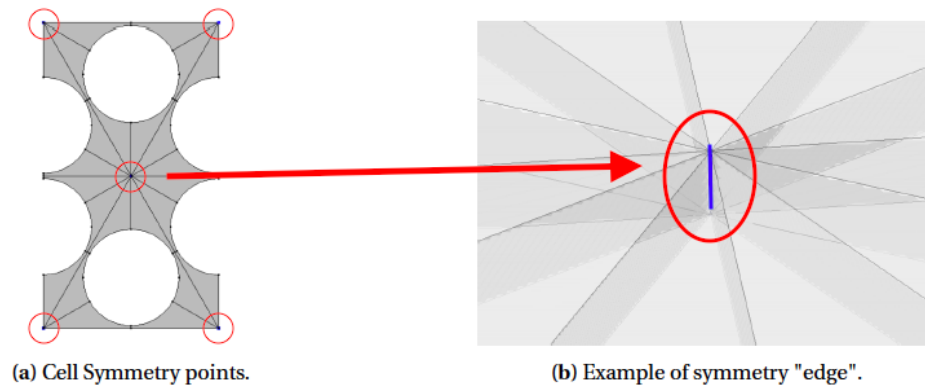


Figure 4.6: Correctly calculated stress distribution of the unit cell, after selecting appropriate fixed points as depicted in Fig. 4.5. Of the original  $\sigma_0 = 1.27\text{GPa}$ , most of it concentrates on the tethers, which presumably decreases the internal loss of the entire structure. This result clearly reproduce those by Tsaturyan et al. [18], and are essential for a correct eigenfrequency analysis of the cell. (Fig. 3.12(b))

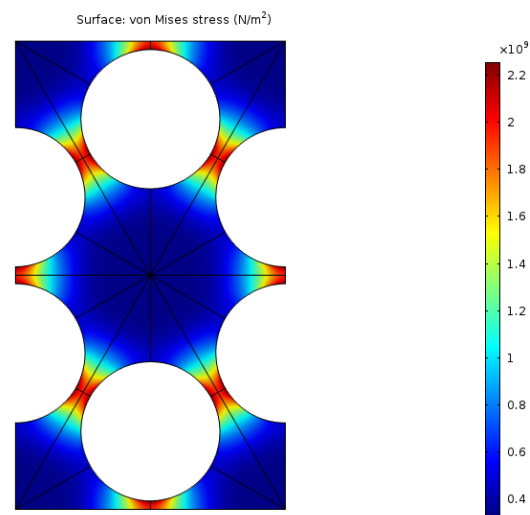
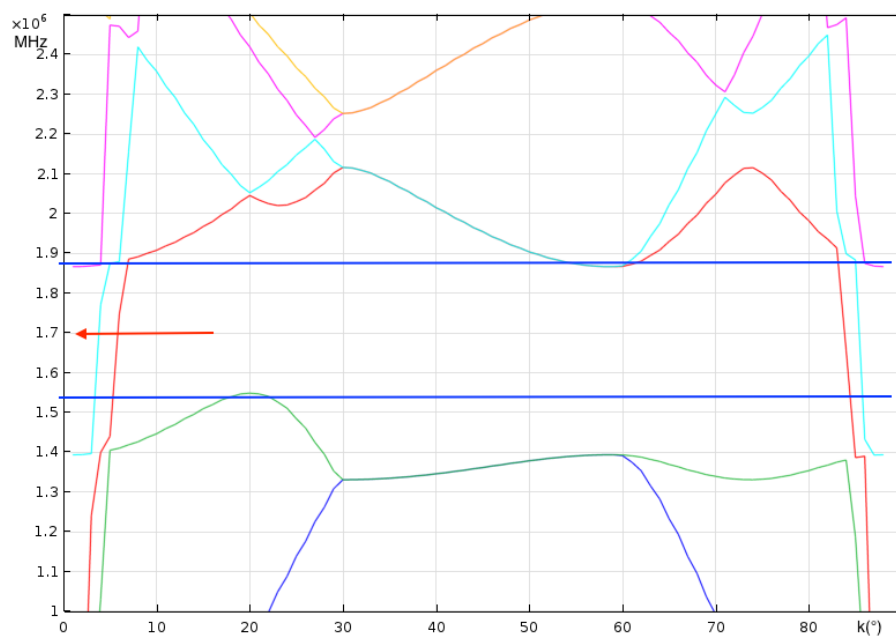


Figure 4.7: Results of the eigenfrequency analysis with Floquet Periodicity, plotted along the  $k$  values in degrees and showing  $f(k) = w(k)/2\pi$  in Hz. The bandgap has the same size and shape of that in Fig. 3.13(a), even though it is shifted upwards by  $\sim 150\text{Hz}$ . The results also show the lateral lines that occur due to the extreme aspect ratio of the unit cell. Nevertheless, despite the bandgap not being perfectly open, its still decreases external loss considerably (see Section 4.4).



infinite structure is fabricated for experimental applications, and the number of cells of a PnC crystal is an important constraint in designing finite structures. For example, in Yu et al. design (Fig. 3.8(a)), the entire structure had to fit in 1cm-across silicon substrate, which limited the maximum number of cells depending on the size of the lattice constant, since a fewer large cells will fit in the space available. For the center bandgap frequency of 3MHz, as shown in Fig. 3.9,  $7 \times 7$  unit cells fit inside the Si substrate, providing good decoupling between membrane and substrate modes [15]. Likewise, for Tsaturyan et al. structure,  $11 \times 19$  cells with  $a = 160\mu\text{m}$  could fit inside the 3mm  $\text{Si}_3\text{N}_4$  membrane (Fig. 3.12) [18].

For our envisioned uses, hybrid PnCs need to be considerably smaller, since we want higher frequency structures that are not as fragile. Tsaturyan et al. [18] have determined the expression for the mid-bandgap frequency as a function of the lattice parameter  $a$

$$f_{\text{band}} = 251\text{Hz} \times a^{-1} \tag{4.1}$$

Which intuitively makes sense, as larger structures would have lower oscillation speeds. We were able to confirm this dependence with COMSOL (compare Fig. 4.8 where  $a = 160\mu\text{m}$  and Fig. 4.9, where  $a = 67\mu\text{m}$ ).

Another way to manipulate the bandgap for this unit cell is to change the size of the cell tether  $w$ . Intuitively, a larger mass difference between the pad and tethers in the cell would result in a larger bandgap. We were able to verify this for smaller cells (Fig. 4.9), but not for larger cells (Fig. 4.8), as the effects seems to not be as pronounced for larger unit cells. Nonetheless, by changing the lattice parameter and the tether width, a range of mid-bandgap frequencies and bandgap sizes can be accessed.

#### 4.4 Flower and Web Designs

Integrating a trampoline defect into a PnC becomes possible with working COMSOL models for the unit cell and a reasonable understanding of how to make arbitrary bandgaps, since we need to make sure that at least one trampoline mode fits inside a trampoline. Unfortunately, the

Figure 4.8: Bandgap Dependence on Cell Tether  $w$  Size for  $a = 160\mu\text{m}$ . The smaller the cell tether width, the lower the midgap frequency  $f_{\text{band}}$ .

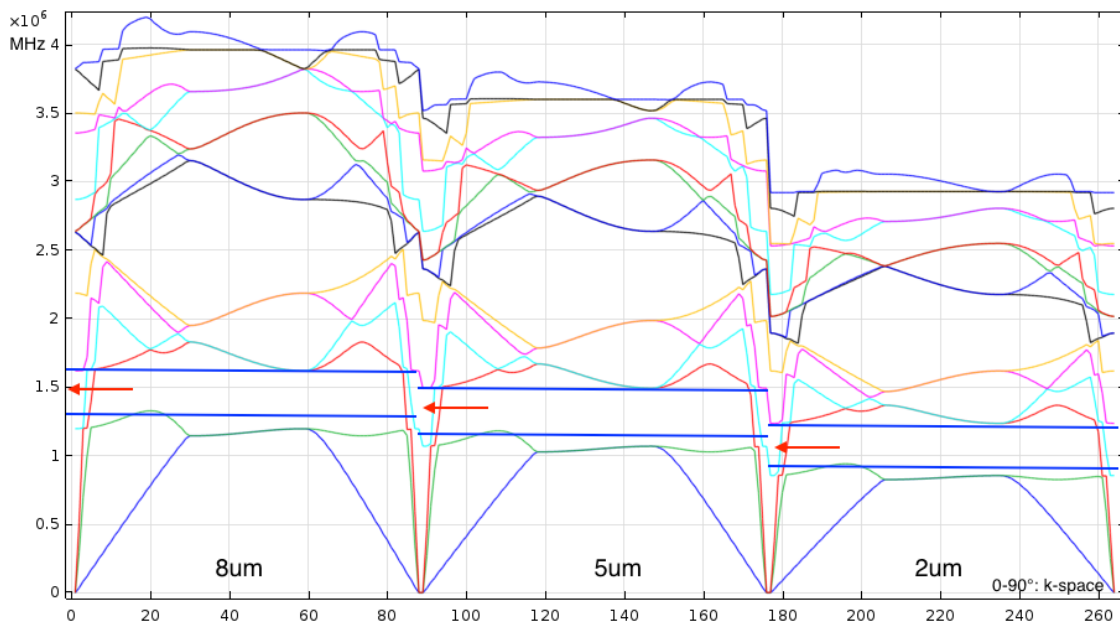
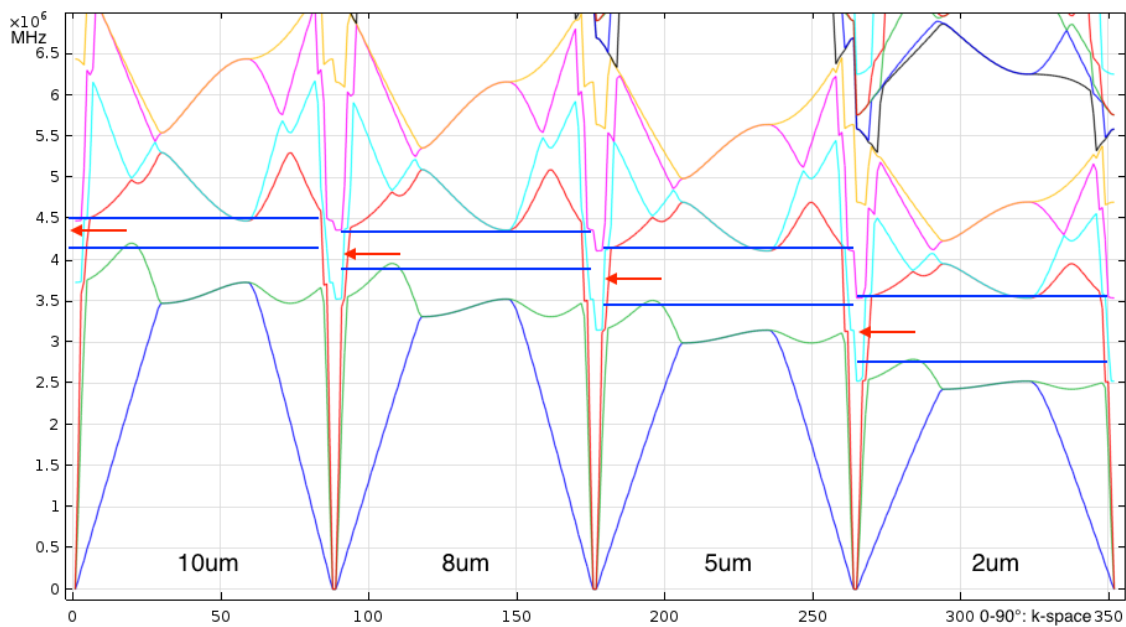


Figure 4.9: Bandgap Dependence on Cell Tether  $w$  Size for  $a = 67\mu\text{m}$ . The smaller the cell tether width, the lower the midgap frequency  $f_{\text{band}}$ .



process is not as easy as simulating a defect-sized trampoline by itself, checking which are its mode frequencies, and then making a bandgap that includes the trampoline mode frequencies. This is likely due to soft-clamping, which will effectively extend the trampoline mode into the PnC, making the resonator larger than it would be (besides making it look different at its ends, since it includes partial unit cells) and changing its modes.

It is important to emphasize, however, that this conjecture was not studied, and the approach in making the designs was more of a tedious trial-and-error approach. One would initially imagine that, because a hybrid PnC is a finite structure, the only way of checking if a in-bandgap trampoline mode exists would be to check each normal mode of the structure one-by-one. Fortunately, we chosen a rather simple parameter that, when plotted against the normal frequencies, clearly indicates where and how big the bandgap is and whether there are any defect modes inside it. This parameter, which is the ratio between the energy in the resonator and the energy in the frames, is discussed in section 4.4.1. The following sections discuss in details the two hybrid-PnCs that we have designed: the small-defect **flower** and the large-defect **web**.

#### 4.4.1 Characterizing a Bandgap in COMSOL

As mentioned previously, to make the search of in-bandgap defect modes more tractable, we define the energy ratio  $E_r$ , which should capture how much of a particular mode's energy is located in the PnC frame, where we assume it will leak out to the substrate. For a defect mode well isolated from external loss, we expect very little of the total energy of the mode to be in either the frame, where it is dissipated, or the PnC cells, where the bandgap prevents energy to be stored. However, for non-defect normal modes that are inside the bandgap, most of the energy should be in the frame, since it cannot be in the PnC cells, nor in the defect.

Let's define this energy ratio  $E_r$  as follows

$$E_r = \frac{U_{\text{defect}}}{U_{\text{frame}}} \quad (4.2)$$

where  $U_{\text{defect}}$  is the energy stored in the defect (Fig. 4.10(a)) and  $U_{\text{frame}}$  is the energy stored in the

frame (Fig. 4.10(b)), defined as

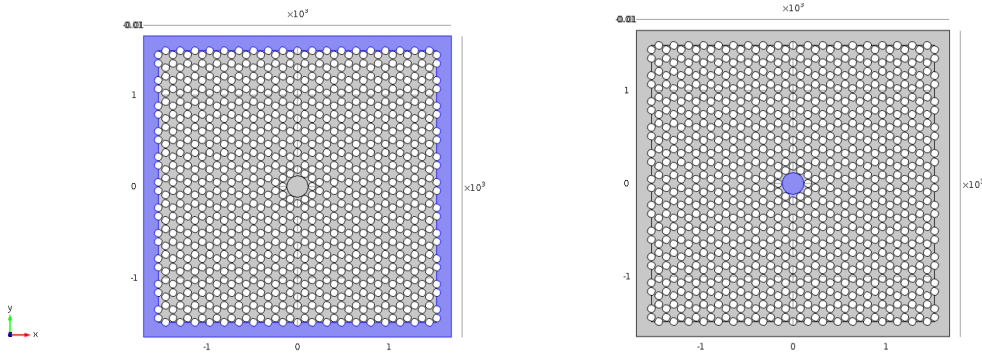
$$U_{\text{defect}} = \int_{V_{\text{defect}}} \rho w(x, y)^2 dV \quad (4.3)$$

$$U_{\text{frame}} = \int_{V_{\text{frame}}} \rho d(x, y)^2 dV \quad (4.4)$$

where  $w$  is the out-of-plane (i.e., along the z-axis) displacement and  $d$  is the total displacement. It is expected that in-bandgap defect modes will exponentially decay away from the center, which results in barely any displacement of the frame. However, for in band-gap modes of the structure that are not defect modes, the PnC will not allow displacement anywhere besides the frame. Thus, the energy ratio for a in-bandgap defect mode  $E_r^d$  will be larger than that for a non-defect in-bandgap energy ratio  $E_r^b$ . Moreover, we expect an out-of-bandgap mode to have about the same displacements in both frame and defect, which implies  $E_r^b$  will also be smaller than the energy ratio for outside of bandgap modes  $E_r^o$ , but  $E_r^o$  will be smaller than  $E_r^d$ :

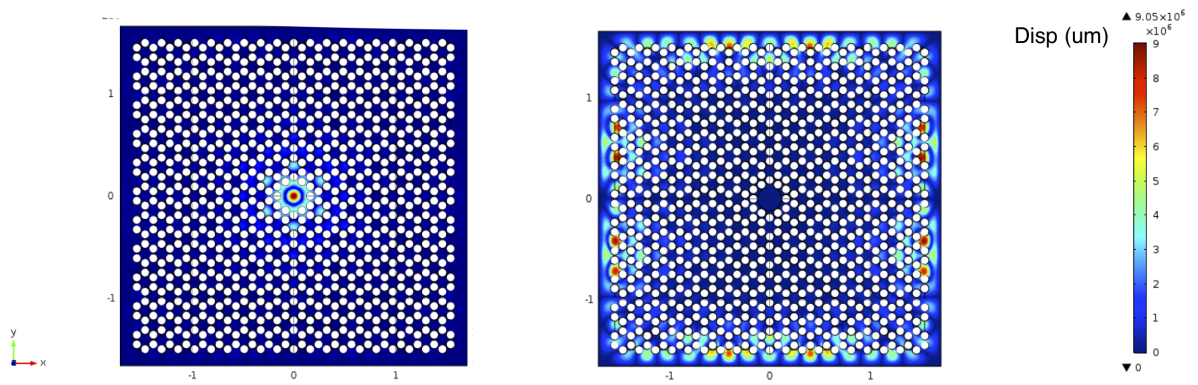
$$E_r^d > E_r^o > E_r^b \quad (4.5)$$

Figure 4.10: A well isolated defect mode will have a much larger displacement field  $w(x, y)$  in the defect than in the frame, since the PnC cell between the two would exponentially dampen the displacements. Therefore, we calculate the ratio of the energy in the two domains to have a indication of how well a particular membrane mode is .



In a plot of the energy ration  $E_r$  versus all the mode frequencies, the bandgap will look like a dip in the  $E_r^b$  values, whereas the in-bandgap defect modes will show as points way above not only

Figure 4.11: COMSOL Results for In-Bandgap Defect Mode and Non-Defect Mode.



the bandgap points, but also the regular, out-of-bandgap  $E_r$  points. For the membrane-like defect PnC published in [18], our energy ratio plot can clearly distinguish bandgap and defect modes 4.12, which gives a convenient, if not fast, way of characterizing hybrid defect-PnC designs.

Even though it may be tempting to think of the defect-modes energy ratios as direct indication of their quality factor, it is important to remember that  $E_r$  does convey any internal loss information. Nonetheless, for the defect modes in particular, it is possible to estimate  $Q = U/\Delta U$  by calculating the total energy lost from bending  $\Delta U$ , given by eq. 3.10, and the total energy  $U$ , given by eq. 3.11. For the five modes in Fig. 4.12, the  $Q$ s calculated in this way relate according to table 4.4.1, which are not related to the energy ratio  $E_r$  values in Fig. 4.12. Unfortunately, we were unable so far to calculate absolute values for  $Q$ , but it remains as a tangible goal in the near future.

Figure 4.12: Our calculations of the energy ratios for a COMSOL model of the 11x19 PnC by Tsaturyan et al [18]. The energy ratio can clearly delineate the bandgap and show the in-bandgap modes, which are colored yellow and labelled A to E.

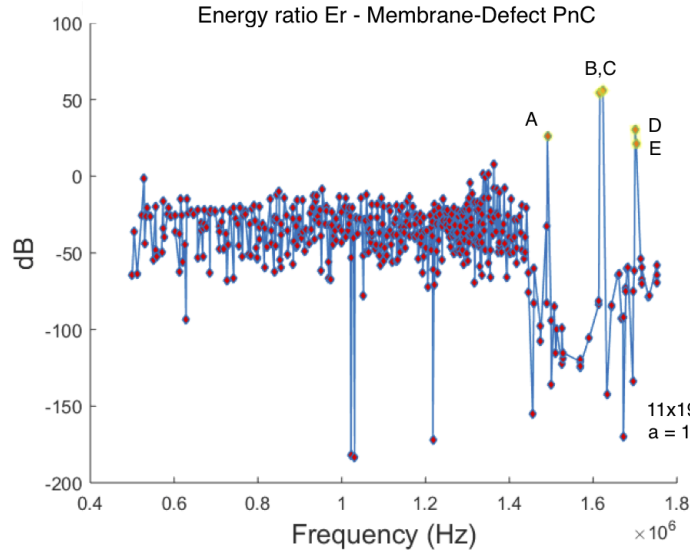


Table 4.4: Mode Q Ratios for the Membrane-Defect PnC.

| Mode ratio | Q ratio |
|------------|---------|
| E/E        | 1       |
| E/D        | 1.22    |
| E/A        | 1.46    |
| E/C        | 3.70    |

#### 4.4.2 Flower

Designing PnC structures with trampolines defects becomes an achievable and manageable goal with a working COMSOL structure models and with a convenient way of characterizing bandgaps and defect modes. Nonetheless, in principle figuring out which particular trampoline design has a in-bandgap mode is more of a guess than it would be practical. Surprisingly, however, the first and most direct attempt in introducing a trampoline defect worked well for our purposes.

This design, called a flower, consists of a hexagonal trampoline of size  $\approx a \times a$  attached to the holes of the adjacent unit cells (Fig. 4.13). The free parameters of the design are the tether width  $W$  and the central pad diameter  $D$ , and the outer fillet radius, denoted  $r$  in Fig. 4.13, was chosen to be equal to the radius of the holes in the PnCs unit cells (see table 4.2 for an expression of  $r$ ).

Initially, we simulated a flower-defect PnC structure with  $11 \times 19$  cells ( $a = 160\mu\text{m}$ ) so that the bandgap and defect modes could be compared to the modes of the membrane-defect PnC. We found that the energy ratios for the normal modes of this structure revealed even better external loss reduction when compared to the membrane-defect PnC structure. However, only the first mode of the trampoline was located inside the bandgap, compared to the five modes of the membrane-defect. Since, as discussed previously, we cannot predict absolute Q values at the moment, a true comparison between trampoline and membrane defects for the same PnC geometry remains to be studied.

Nevertheless, we are more interested in smaller PnC structures with up to  $1\text{mm}$  length on the side, and with defect mode frequency  $f_{\text{defect}} = \omega/2\pi \sim 1.5\text{MHz}$ , so they can be more robust

Figure 4.13: A flower trampoline-defect consists of a six-tethered trampoline with size  $\sim a \times a$ , where  $a$  is the size of the unit cell. The flower defect itself has two free parameters: tether width  $W$  and central pad diameter  $D$ . The outer fillet radius  $r$  is the same as the radius of the holes in the PnC unit cells.

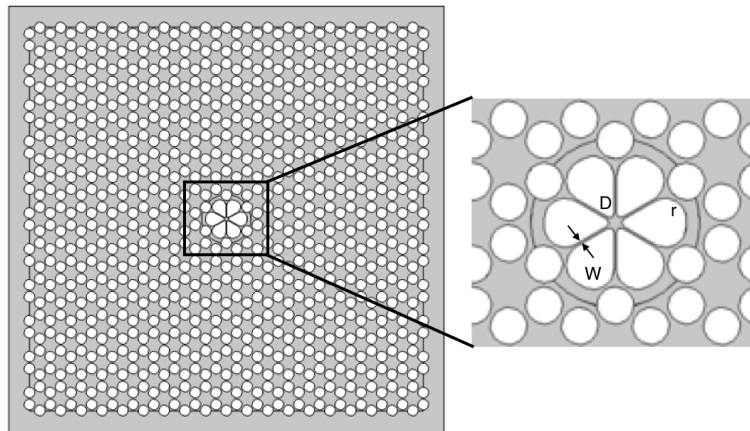
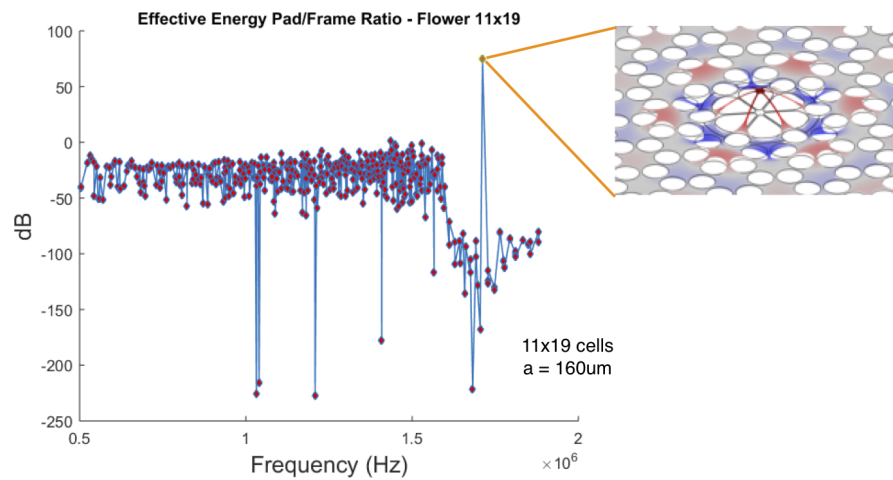


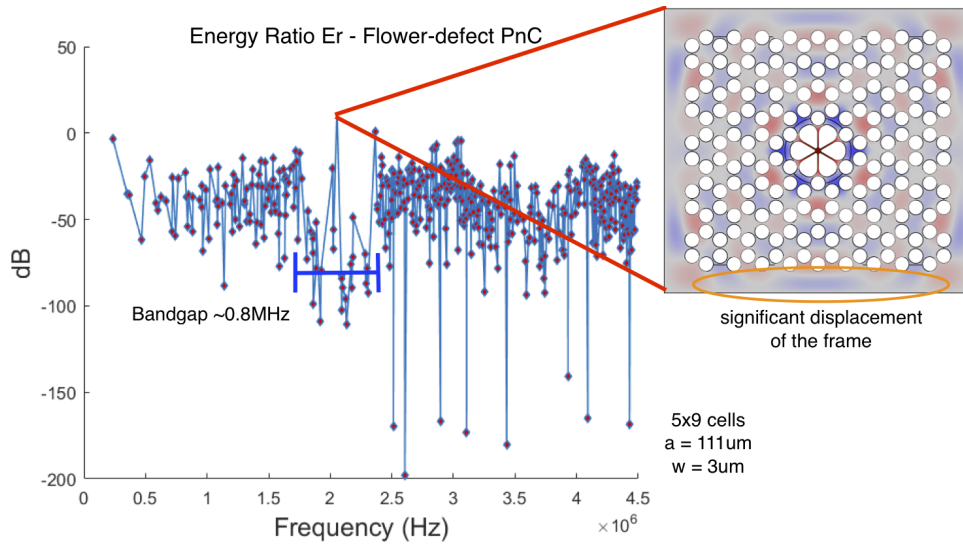
Figure 4.14: Our simulations for the flower-defect PnC with  $11 \times 19$  cells ( $a = 160\mu\text{m}$ ) show a unique, very-well isolated, in-bandgap defect mode.



and work better with cavities. By reducing the cell size, we can get more unit cells and guarantee a better defect mode isolation, but if this would increase the mid-bandgap frequency of the structure. A compromise has to be made such that there are enough cells to decrease dissipation, but also both the size and the bandgap frequencies are within the desired values.

After trying a few combinations, the best flower-defect PnC found is a  $5 \times 9$ ,  $a = 111\mu\text{m}$  PnC structure with unit cell tether width of  $w = 3\mu\text{m}$ , which increased the bandgap enough for a mode to fit inside at  $f_{\text{flower}} \approx 2\text{MHz}$ . Unfortunately, the energy ratio plot indicates this structure barely isolates the defect mode from the frame, which is corroborated by COMSOL results for the displacement in the structure (Fig. 4.15).

Figure 4.15: The best flower design with  $5 \times 9$  cells and that is small enough ( $< 1\text{mm}$ ) with bandgap frequencies around  $2\text{MHz}$  is not as well insulated from external loss as the much bigger  $11 \times 19$  design. Nonetheless, this design has a bandgap and a defect mode, even if not entirely decoupled from the frame.

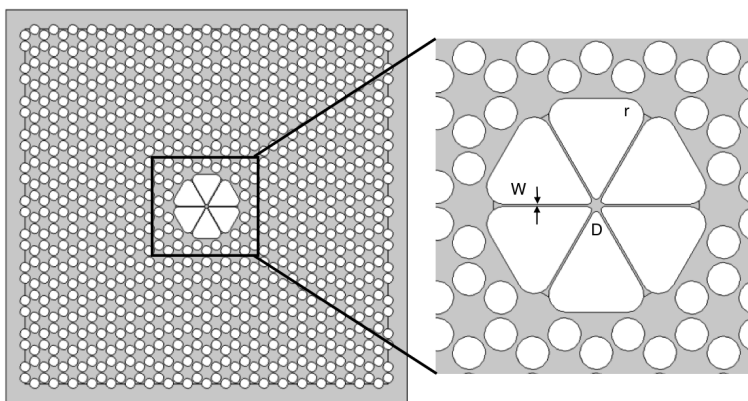


#### 4.4.3 Web

A natural complement to the flower-defect is a larger hexagonal trampoline defect which has higher-order modes inside the bandgap, instead of just the one in-bandgap first mode of the

flower. After trying a few different configurations, a working larger-trampoline defect was designed, obtaining the web geometry. Similarly to the flower, the web consists of six tethers connected to the adjacent PnC unit cells. In this design, the web defect is twice as big as the flower, spanning two unit cells ( $\approx 2a \times 2a$  in size). The free parameters are the same as in the flower, i.e., tether width  $W$  and pad diameter  $D$ , with the outer filler radius  $r$  fixed to the value of the unit cell  $r$  (Fig. 4.16).

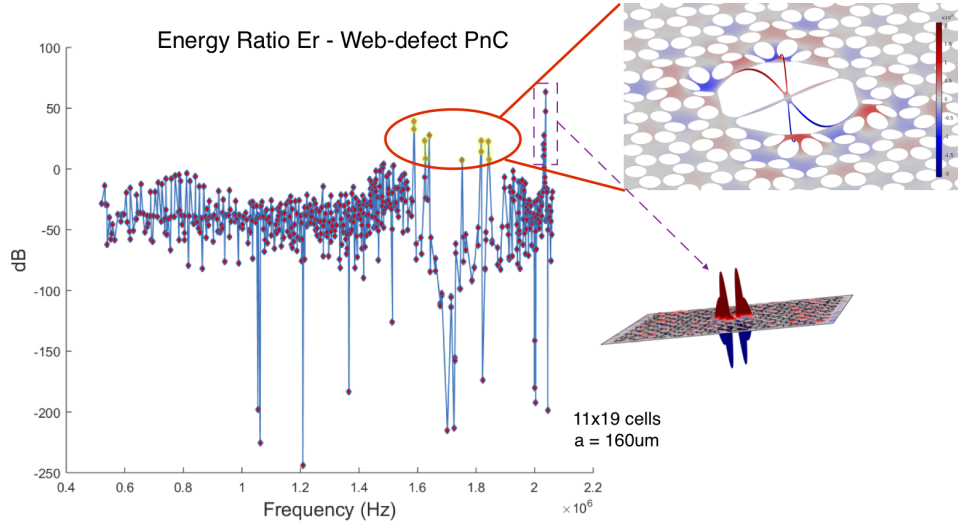
Figure 4.16: A web trampoline-defect consists of a six-tethered trampoline with size  $\sim 2a \times 2a$ , where  $a$  is the size of the unit cell, being essentially a bigger version of the flower. Thus, like the flower defect, the web has two free parameters: tether width  $W$  and central pad diameter  $D$ . The outer fillet radius  $r$  is the same as the radius of the holes in the PnC unit cells.



Again, we compare the energy ratio of the web modes in a  $11 \times 19$  PnC with the membrane-defect PnC. For the web there are many higher order modes in the bandgap, as desired, but all are somewhat less isolated than the flower mode or the modes of the membrane-defect PnC (Fig. 4.17). One possible explanation for this is that, being for times as large than a flower defect, the web reduces the effective number of unit cells in the PnC, which decreases the attenuation of in-bandgap normal modes of the whole structure. COMSOL also calculated a few spurious, completely unphysical modes, which seem to be the membrane stretching upwards, creating big  $\text{Si}_3\text{N}_4$  “flaps.” It is unclear what causes such modes to appear, but luckily any normal modes outside the bandgap are not of interest or relevant to our design considerations, so we can be reasonably confident this

particular simulation gives the actual in-bandgap web modes.

Figure 4.17: The Web-defect PnC with  $11 \times 19$  cells ( $a = 160\mu\text{m}$ ) has several in-bandgap defect mode, all less decoupled from the frame than the flower mode.



In fact, the larger size of the web makes it less suited for small structures with  $\sim 1.5\text{MHz}$  mid-bandgap frequencies. If a web defect is inserted into a  $5 \times 9$  PnC, the remaining number of cells is too small to form a bandgap, even though it is still possible to identify the web modes among the other, non-defect normal modes of the structure 4.18.

Nonetheless, we can use the web to access higher frequency defect-modes by using it in a PnC with smaller unit cells. In particular, we found that by making  $a = 67\mu\text{m}$  and  $w = 2\mu\text{m}$ , we can have a  $9 \times 15$  structure that opens a  $\sim 0.8\text{MHz}$  bandgap with several web-defect modes 4.19. Moreover, compared to the  $5 \times 9$  flower PnC, this web PnC design has a significantly better in-bandgap defect modes, with less displacement induced at the frame.

Figure 4.18: Inserting a web defect in a  $5 \times 9$  PnC erases any PnC attenuation effects of in-bandgap normal modes.

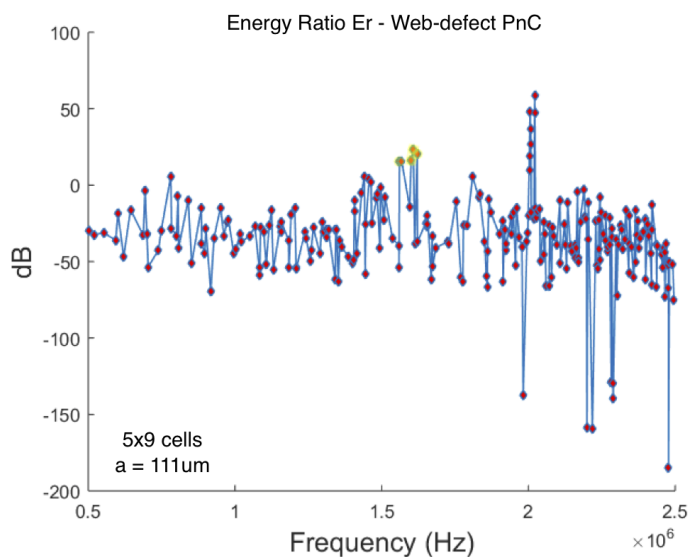
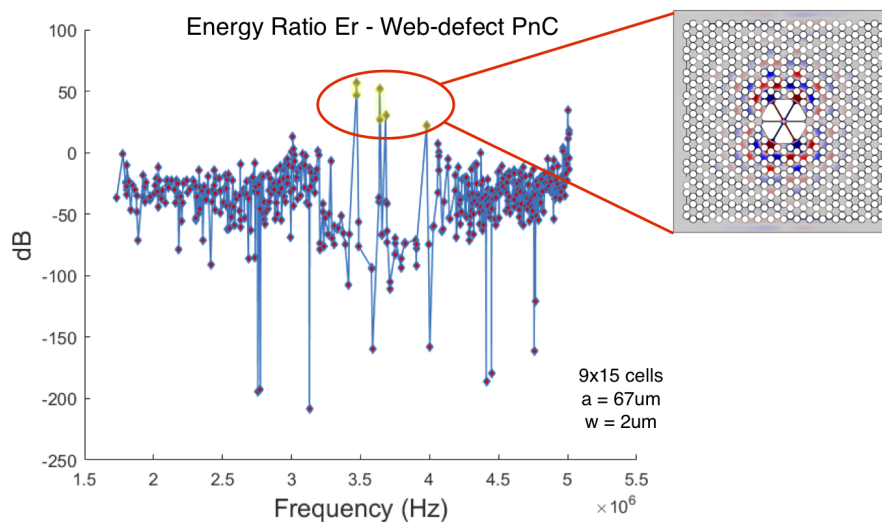


Figure 4.19: By making a PnC with smaller  $a = 67\mu\text{m}$  cells and thinner cell tethers with  $w = 2\mu\text{m}$ , several web modes appear inside a significantly broad bandgap that opens for a  $9 \times 15$  unit cells. Because, compared to the flower design, this web PnC has more unit cells, the web modes inside the bandgap are better insulated against external losses, as can be seen in the inset.



## Chapter 5

### Modeling Optical Absorption for Si<sub>3</sub>N<sub>4</sub>

#### 5.1 Introduction

In chapter 2 we discussed how the optomechanical effects could be increased with a more intense intra-cavity field, that is, with more photons inside the cavity interacting with the resonator. The ultimate goal is to have  $g_0$  significant compared to the systems mechanical decay rate  $\Gamma_M$  and optical decay rate  $\kappa_c$ . Increasing the light intensity is a way to compensate for the optical decay, increasing the number of optomechanical interactions per decay “cycle.”

Intuitively, increasing the number photons in a cavity will increase the photon-backaction on the membrane, i.e., how big the brownian motion of a membrane will be in the intracavity “photon fluid.” Clearly, as discussed in chapter 2, the average thermal occupancy of the resonator needs to be below zero, i.e.  $\bar{n}_t h < 1$ , for such effects to be observed. In principle, this requirement would place a limit in how many photons could be inserted in the cavity, since the resonator will end up absorbing some of the light, and heating up, i.e., the light will create phonons in the resonator, taking it out of the ground state if the rate of absorption is high enough. Therefore, in the experiment where the photon backaction limit is observed [6], one concludes that the absorption of Si<sub>3</sub>N<sub>4</sub> needs to be exceedingly small.

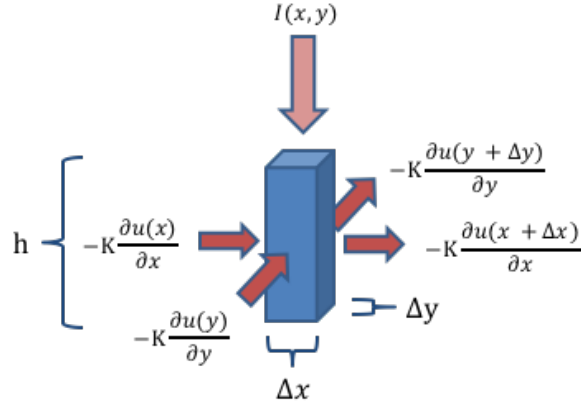
This chapter describes a heat equation model used to provide an lower bound on the optical absorption for Si<sub>3</sub>N<sub>4</sub>, given literature values for the thermal conductivity at cryogenic temperatures and temperature vs power data points for different experiments.

## 5.2 Heat Equation Modeling

Let's start by deriving a 2D heat equation for a square membrane illuminated by a Gaussian beam. The goal is to obtain the steady-state temperature distribution as a function of optical absorption  $A_{\text{opt}}$ , and then compare the maximum temperature the model reaches, as a function of laser input power  $P_{\text{in}}$ , with measured membrane and string temperatures.

In deriving a heat equation, we consider a 2D infinitesimal membrane element of height  $h$ , which corresponds to the membrane thickness. Energy enters the membrane element from the sides due to thermal conductivity, and each membrane element also gains energy from the gaussian beam of intensity  $I(x, y)$ .

Figure 5.1: Energy balance of a 2D infinitesimal membrane element illuminated by a gaussian beam of intensity  $I(x, y)$ . The beam injects energy into the elements, which also comes from the sides through thermal conductivity.



Using the parameters of table 5.1, the change in the energy of the infinitesimal membrane segment is given by the heat balance across  $\Delta x$  and  $\Delta y$  and the heat source due to the absorbed light of the laser beam

$$c\rho \times \Delta x \Delta y h \times (u(x, y, t + \Delta t) - u(x, y, t)) = \Delta t \times h \Delta y \times K \left( \frac{\partial u(x + \Delta x)}{\partial x} - \frac{\partial u(x)}{\partial x} \right) \quad (5.1)$$

$$+ \Delta t \times h \Delta x \times K \left( \frac{\partial u(y + \Delta y)}{\partial y} - \frac{\partial u(y)}{\partial y} \right) \quad (5.2)$$

$$+ \Delta t \times h \Delta x \Delta y \times \frac{(A_{\text{opt}} I(x, y))}{h} \quad (5.3)$$

Table 5.1: Parameters of the Heat Equation.

| Parameter        | Description              |
|------------------|--------------------------|
| $u(x, y, t)$     | temperature distribution |
| $c$              | heat capacity            |
| $\rho$           | mass density             |
| $h$              | membrane thickness       |
| $K$              | thermal conductivity     |
| $A_{\text{opt}}$ | optical absorption       |
| $I(x, y)$        | laser intensity          |

We divide the heat balance equation by  $h\Delta x\Delta y\Delta t$  to get

$$c\rho \times \left( \frac{u(x, y, t + \Delta t) - u(x, y, t)}{\Delta t} \right) = \frac{K}{h} \left( \frac{\left( \frac{\partial u(x+\Delta x)}{\partial x} - \frac{\partial u(x)}{\partial x} \right)}{\Delta x} \right) \quad (5.4)$$

$$+ \frac{K}{h} \left( \frac{\left( \frac{\partial u(y+\Delta y)}{\partial y} - \frac{\partial u(y)}{\partial y} \right)}{\Delta y} \right) \quad (5.5)$$

$$+ \frac{(A_{\text{opt}}I(x, y))}{h^2} \quad (5.6)$$

And, by using the limits  $\Delta t, \Delta x, \Delta y \rightarrow 0$ , we get the time-dependent heat equation for the 2D membrane under laser light of intensity  $I(x, y)$

$$c\rho \frac{\partial u(x, y, t)}{\partial t} = \frac{K}{h} \frac{\partial^2 u(x, y, t)}{\partial x^2} + \frac{K}{h} \frac{\partial^2 u(x, y, t)}{\partial y^2} + \frac{A_{\text{opt}}}{h} I(x, y) \quad (5.7)$$

Naturally, we are interested in the steady state solution, as discussed in the introduction. Thus, we make  $\partial u/\partial t = 0$  and substitute the expression for the intensity of a Gaussian beam of waist  $\omega_0$  and power  $P$ :

$$\frac{\partial^2 u(x, y)}{\partial x^2} + \frac{\partial^2 u(x, y)}{\partial y^2} = -\frac{A_{\text{opt}}}{K} \times \frac{1}{h} \times \frac{2}{\pi \omega_0^2} \exp\left(\frac{-2(x^2 + y^2)}{\omega_0^2}\right) \quad (5.8)$$

Equation 5.8 shows reasonable behavior: if power is increased or absorption are increased, the temperature distribution curvature increases, indicating a larger heating peak. On the other hand, if the thermal conductivity is increased, or the beam waist, the temperature curvature decreases, indicating a lower peak temperature.

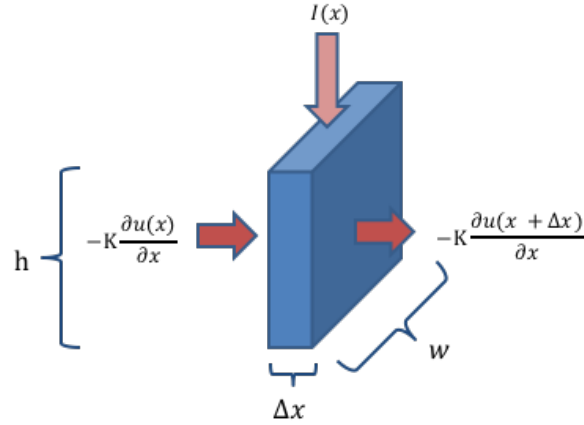
In solving the 2D heat equation, we assume that the membrane boundaries are at constant  $u(x, y) = 0$  temperature, i.e., all of the heat diffuses perfectly in the substrate without heating

it. Moreover, because we are looking for a lower bound on the optical absorption  $A_{\text{opt}}$ , we are really interested in only the peak temperature of the distribution  $u(x, t)$ . Thus, to simplify the numerical solution, we transform eq. 5.8 to polar coordinates and solve it using the numerical ODE solvers in MATLAB, since  $u(r = L/2) = 0$  is a good approximation of the constant boundary conditions if the beam waist is considerably smaller than the membrane side length  $L$ .

$$\frac{\partial^2 u(r)}{\partial r^2} + \frac{1}{r} \frac{\partial u(r)}{\partial r} = -\frac{A_{\text{opt}}}{K} \times \frac{1}{h} \times \frac{2P}{\pi \omega_0^2} \exp\left(\frac{-2(r^2)}{\omega_0^2}\right) \quad (5.9)$$

Similarly, we follow the same derivation process to obtain a 1D heat equation to model the heating of a  $\text{Si}_3\text{N}_4$  tether under illumination, which is necessary if we are to use the heating data of  $\text{Si}_3\text{N}_4$  tethers and strings, for instance. As before, we start with a 1D infinitesimal element and write down its energy change in time  $\Delta t$

Figure 5.2: Energy balance of a 1D infinitesimal tether element illuminated by a gaussian beam of intensity  $I(x)$ . The beam injects energy into the elements, which also comes from the sides through thermal conductivity.



$$c\rho \times wh\Delta x \times (u(x, t + \Delta t) - u(x, t)) = \Delta t \times hw \times K \left( \frac{\partial u(x + \Delta x)}{\partial x} - \frac{\partial u(x)}{\partial x} \right) \quad (5.10)$$

$$+ \Delta t \times hw\Delta x \times \frac{(A_{\text{opt}}I(x, y))}{hw} \quad (5.11)$$

Where  $w$  is the tether's width. Dividing by  $hw\Delta x\Delta t$  and applying the limits  $\Delta t, \Delta x \rightarrow 0$  we

get

$$c\rho \times \frac{\partial u(x, t)}{\partial t} = \frac{K}{x} \frac{\partial^2 u(x)}{\partial x^2} + A_{\text{opt}} \frac{I(x)}{hw} \quad (5.12)$$

The steady state solution  $\partial u/\partial t = 0$  is

$$\frac{\partial^2 u(x)}{\partial x^2} = -\frac{A_{\text{opt}}}{K} \frac{I(x)}{hw} \quad (5.13)$$

For which we need the 1D intensity expression of the laser beam. A requirement is that integrating  $I(x)$  over all 1D space has to give the total power on the membrane:  $\int_{-\infty}^{\infty} I(x)dx = P$ . Therefore

$$I(x) = \sqrt{\frac{2}{\pi}} \frac{P}{\omega_0} \exp\left(\frac{-2x^2}{\omega_0^2}\right) \quad (5.14)$$

And the final 1D steady state heat equation for a tether under a “1D” Gaussian beam of waist  $\omega_0$  and power  $P$  is

$$\frac{\partial^2 u(x)}{\partial x^2} = -\frac{A_{\text{opt}}}{K} \frac{1}{hw} \sqrt{\frac{2}{\pi}} \frac{P}{\omega_0} \exp\left(\frac{-2x^2}{\omega_0^2}\right) \quad (5.15)$$

### 5.3 Cryogenic Thermal Conductivity Values

In order to estimate the minimum optical absorption of  $\text{Si}_3\text{N}_4$  that fits measured heatings due to laser light, we need thermal conductivity values  $K$ , specifically at the temperatures corresponding to experiments.

A first concern in determining the thermal conductivity of  $\text{Si}_3\text{N}_4$  at cryogenic temperatures would be to figure out if the *quantization of thermal conductance* is of importance. If we consider a tether connecting two heat reservoirs at different temperatures, the conductance between the two decreases as the cross-sectional area of the tether decreases. It would be reasonable to expect that this relation is smooth all the way to zero conductance at zero cross-sectional area, but this is not true. There is a minimum of thermal conductance that each phonon of the tether carries, which means a tether of non-zero cross-sectional area will always correspond to a minimum thermal conductance. A quasi one-dimensional tether will have a minimum of four phonon (one dilation lattice mode, one torsional, and one flexural mode for each cross-sectional dimension), which will carry each a thermal conductance phonon. As the dimensions of the cross-sectional are of the tether

are increased, more phonons can fit inside, to a point where adding a new phonon is virtually negligible to the conductance. In order to know if thermal conductance, and therefore thermal conductivity, is relevant, we have to check how comparable are the geometrical dimensions of our resonators thermal contact to the bath and the wavelength of phonons at the bath temperature.

We can estimate the wavelength of a phonon of lattice vibration under certain temperature as follows

$$\lambda_{\text{phonon}} \sim \frac{h\sqrt{\frac{E}{\rho}}}{k_b T} \quad (5.16)$$

where  $h$  is Planck constant,  $E$  is the young's modulus, and  $\rho$  is the resonator's mass density. The effects of thermal conductance quanta become relevant when  $\lambda_{\text{phonon}} \sim w$ , where  $w$  is the width of the thermal contact between bath and resonator [35]. For the smallest bath temperatures  $T = 40\text{mK}$  we achieve in the experiments described in section 5.4, the equivalent wavelength

$$\lambda_{\text{phonon}} \sim \frac{h\sqrt{\frac{E}{\rho}}}{k_b(T = 40\text{mK})} \approx 10\mu\text{m} \quad (5.17)$$

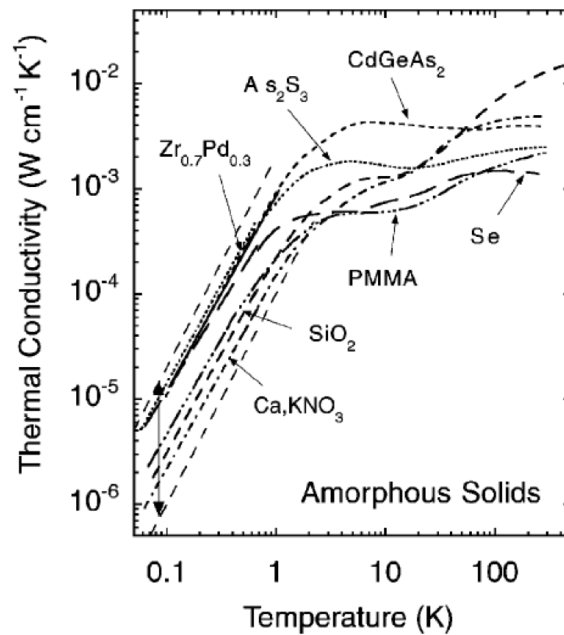
is considerably smaller than the membrane cross-sectional length of  $500\mu\text{m}$ . This indicates that for membrane there's "plenty of room" for phonon modes. However, for trampoline geometries discussed in chapter 4, the quantization of thermal conductance is definitely relevant, as the width  $w$  of trampoline tethers was smaller than the  $\lambda_{\text{phonon}}$ .

Therefore, the 1D heat-equation of section 5.2, which assumes thermal conductivity as a purely material property and a correspondingly smooth thermal conductance, will inevitably lead to unreasonable results if the tether length is similar to the typical phonon wavelengths. The 2D equation, however, is justified for membrane heating since the typical  $500\mu\text{m} \times 500\mu\text{m}$  membrane sizes is considerably larger than the phonon wavelengths. Thus, the analytical heat equation solutions can be pursued by using available values of thermal conductivity  $K$ .

Unfortunately, measured values of cryogenic thermal conductivity of silicon nitride are still scarce, specially at milikelvin temperatures. In fact, there are no measurements of the thermal conductivity of high-stress silicon nitride at cryogenic temperatures. Nevertheless, it is possible to extrapolate from measured low stress silicon nitride values for a couple different reasons. First,

silicon nitride is an amorphous solid, and all amorphous solids have  $K(T) \propto T^2$  for  $T < 1\text{K}$ , as seen in Fig. 5.3. This indicates that at millikelvin temperatures the thermal conductivity will be very small, enhancing heating of SiN devices under laser light, which supports the notion that their optical absorptions need to be exceedingly small for the observation of quantum backaction from an intense intracavity field.

Figure 5.3: Thermal Conductivity of Amorphous Solids is quadratic with  $T$  for cryogenic temperatures (Image credit: Pohl et al. [36])



The  $K(T) \propto T^2$  behavior was somewhat confirmed by Leivo and Pekola [37], who measured the thermal conductivity of membrane- and trampoline-like low-stress SiN devices for temperatures from  $T = 70\text{mK}$  to  $T = 1\text{K}$  (table 5.2). Unfortunately, the strong geometrical dependence of these values suggest a not-perfect adequacy of the derived heat eqs. 5.9 and 5.15. Nonetheless, the expressions in table 5.2 were the only ones found in literature.

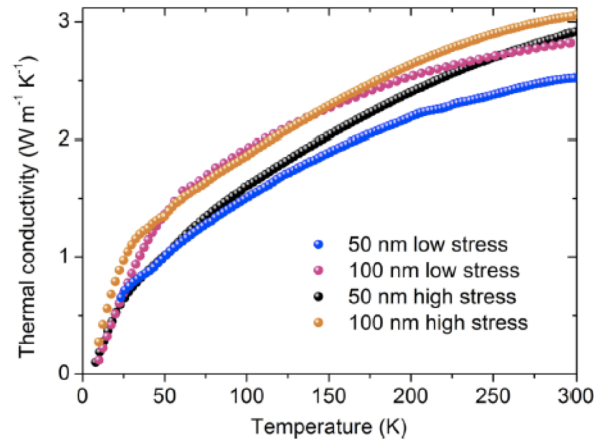
It is not obvious that the thermal conductivity of high-stress silicon nitride should follow the results of Leivo and Pekola, but Ftouni et al. [38] have measured converging thermal conductivities for low and high stress SiN at cryogenic temperatures, which allows for the use of Leivo and Pekola's

Table 5.2: Thermal Conductivity Expressions for SiN at mK Temperatures.

| Device                                      | Thermal Conductivity $K(T)$ (W/mK) |
|---|------------------------------------|
| Membrane-like [37]                          | $(1.45 \times 10^{-2})T^{1.8}$     |
| Trampoline-like [37]                        | $(1.58 \times 10^{-3})T^{1.58}$    |
| Membrane-like (Holmes et al. (unpublished)) | $(1.62 \times 10^{-2})T^{2.5}$     |

results in our heat equation models.

Figure 5.4: The thermal conductivity of both stress variants of silicon nitride converge to the same values at cryogenic temperatures (Image credit: Ftouni et al. [38])



Together with some measurements by Zink and Hellman [39], we can select a few useful thermal conductivity values, used in sections 5.4.2 and ?? below.

Table 5.3: Thermal Conductivity Values for SiN at Cryogenic Temperatures.

| Temperature (K) | Thermal Conductivity $K$ (W/mK) [39] |
|-----------------|--------------------------------------|
| 5               | 0.13                                 |
| 3               | 0.07                                 |

Because at cryogenic temperatures silicon nitride's thermal conductivity behaves like those of amorphous solid, but the results by Leivo and Pekola are geometry-dependent, we compromise and chose the most reliable result based on it being the closest geometry <sup>1</sup>:  $K(T) = (1.45 \times 10^{-2})T^{1.8}$ .

We can then substitute this value into the heat equations 5.9 and 5.15 and get a thermal ratio  $R$

<sup>1</sup> Homes et al. unpublished result was measured for a very thick SiN circular slab, which makes it less adequate compared to Leivo and Pekola's 400nm-thick square membrane.

defined as

$$\frac{A_{\text{opt}}}{K(T)} = \frac{A_{\text{opt}}}{1.45 \times 10^{-2} T^{1.8}} = \frac{R}{T^{1.8}} \Rightarrow R = \frac{A_{\text{opt}}}{1.45 \times 10^{-2}} \quad (5.18)$$

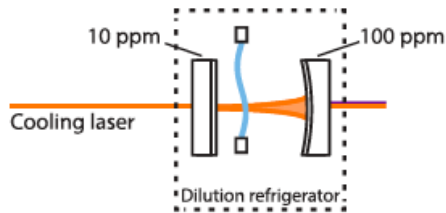
This way, we can plot several Maximum heating versus Optical Power relations for different  $A_{\text{opt}}$  and discover what minimum absorption explains experimentally observed heating.

## 5.4 Lower-bounds on Optical absorption

### 5.4.1 1064nm light at Milikelvin Temperatures

Our first experimental data point comes from Peterson et al. [6] measurement of the quantum back-action limit for a Si PnC membrane resonator at 40mK and 100mK. According to the authors, the setup consisted of a Fabry-Pérot cavity of Finesse  $\sim 30000$ , which corresponds to  $N \approx F/\pi = 10000$  photon reflections (Fig. 5.5). Therefore, the power incident on the membrane was  $10^4$  greater than the input power, resulting in  $P = 1\text{mW}$ .

Figure 5.5: By having a high-finesse cavity, enough optical power, and a high-Q membrane-resonator, Peterson et al. were able to measure the quantum-backaction of the membrane. The inferred heating of the membrane, obtained from a thermometry measurement beyond the scope of this thesis (see [6]), was of 100mK (Image credit: Peterson et al. [6]).



Using eq. 5.9 with  $R$  given by 5.18, the observed steady-state heating of the membrane correspond to a **minimum optical absorption of slightly less than  $10^{-8}$**  (Fig. 5.6), which is 4 orders of magnitude smaller than for low-stress silicon nitride membranes [8].

Figure 5.6: Maximum Temperature on Membrane vs. Optical Power plots for different optical absorption values and with  $T_{\text{base}} = 40\text{mK}$ . The selected point shows how the 2D model peak temperature is close to the observed values in table 5.4.

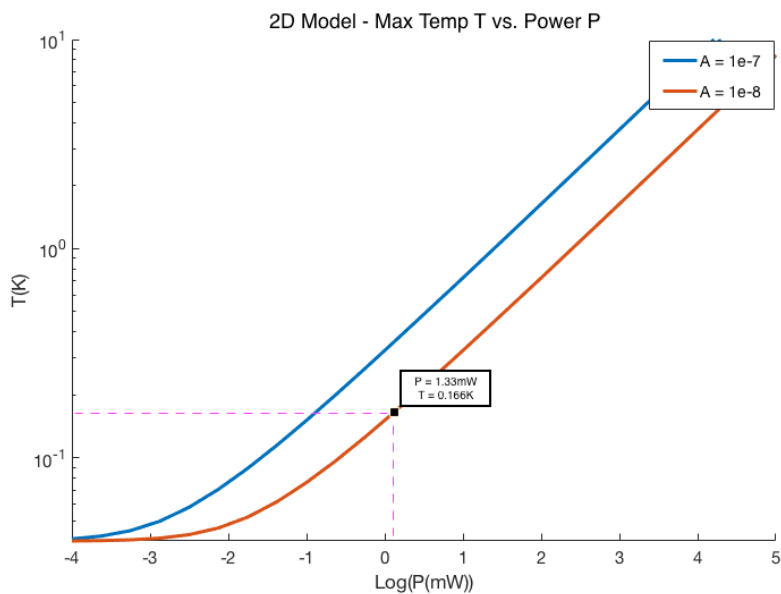


Table 5.4: Heating of Si<sub>3</sub>N<sub>4</sub> at Milikelvin Temperatures.

| Base Temperature (mK) | Heating (mK) |
|-----------------------|--------------|
| 40                    | +100mK       |
| 100                   | +100mK       |

### 5.4.2 1064nm light at Cryogenic Temperatures

Another data point for Si<sub>3</sub>N<sub>4</sub> heating comes from the optomechanical squeezing of light experiment [27]. In this case, the base temperature was  $T_{\text{base}} = 4.6\text{K}$ , the input power was  $P_{\text{in}} = 110\mu\text{W}$ , and the membrane thickness was  $h = 40\text{nm}$ . Using the the mirror transmission  $R = 10^{-4}$  and number of photon reflections  $N = F/\pi = \sqrt{R}/(1 - \sqrt{R})$ , the power on the membrane was  $P = 1.1\text{W}$ .

Here, we have to use the thermal conductivity value for  $T = 5\text{K}$  in table 5.3, such that

$$K(5K) = 0.13 \frac{\text{W}}{\text{mK}} = (\beta)(5\text{K})^{1.2} \Rightarrow \beta = 5.2 \times 10^{-3} \quad (5.19)$$

and the ratio R becomes

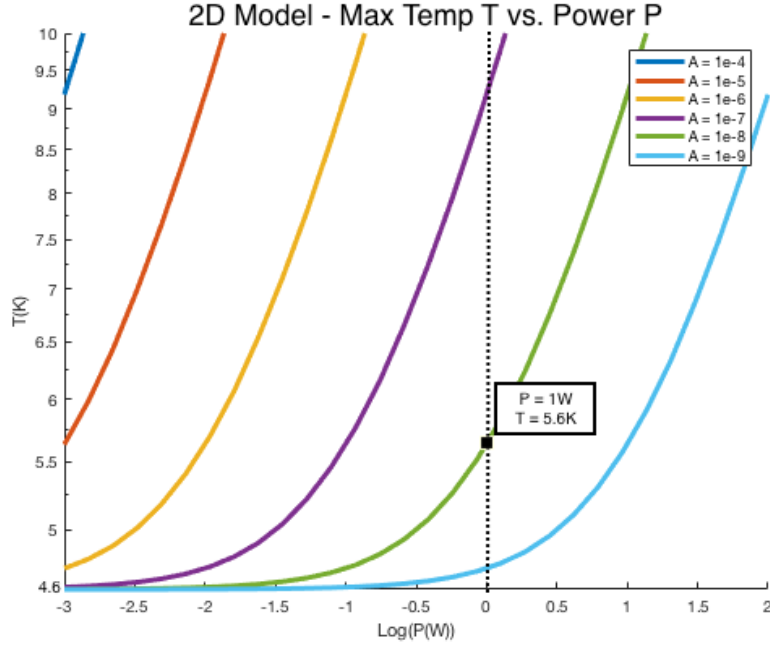
$$R = \frac{A_{\text{opt}}}{\beta} = \frac{A_{\text{opt}}}{5.2 \times 10^{-3}} \quad (5.20)$$

According to the 2D heat equation solutions for this particular R, all **optical absorptions above  $10^{-9}$  produce too much heating**, since barely no heating was observed (according to my conversations with one of the authors), which contradicts section 5.4.1.

### 5.4.3 904nm light at Milikelvin Temperature

A more recent experiment measured the mode ringdown times as a function of input power and base temperature. The setup consisted of an 904nm laser-illuminated Si PnC membrane inside a high-finesse cavity for 1064nm light. Using a network analyzer and piezos, several membrane modes were excited and then detected via interferometry. By disconnecting the network analyser, the ringdown time  $\tau = 2\pi/Q$  of each mode can be measured. In order to enhance the effects of heating, the measurements were made at milikelvin temperatures, where thermal conductivity is

Figure 5.7: Maximum Temperature on Membrane vs. Optical Power plots for different optical absorption values and with  $T_{\text{base}} = 4.6\text{K}$ . The selected point shows that an optical absorption of  $10^{-8}$  is too high to explain the experimentally observed negligible heating above the base temperature.



very small and the effects of the absorption of optical power should be of greater resolution (and it is also the temperature regime of biggest interest).

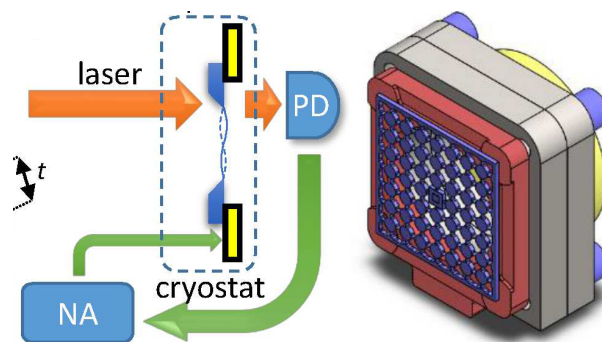
Dr. Ran Fischer fitted the  $Q \times P$  and  $Q \times T_{\text{base}}$  data and obtained a relation  $T \times P$ , which I used to compare to the maximum heating from the 2D model.

$$T(P) = (P \times 10^{8.26})^{\frac{1}{4.26}} \quad (5.21)$$

For fitting results from the 2D model to this equation, we can simply choose an arbitrary  $P$  value and compare the  $T(P)$  value from the experimental fit (5.21) to the maximum  $u(r)$  the model produces. In particular, choosing  $P \sim 1\text{W}$  corresponds to  $T \sim 390\text{mK}$  for a  $T_{\text{base}} = 40\text{mK}$ .

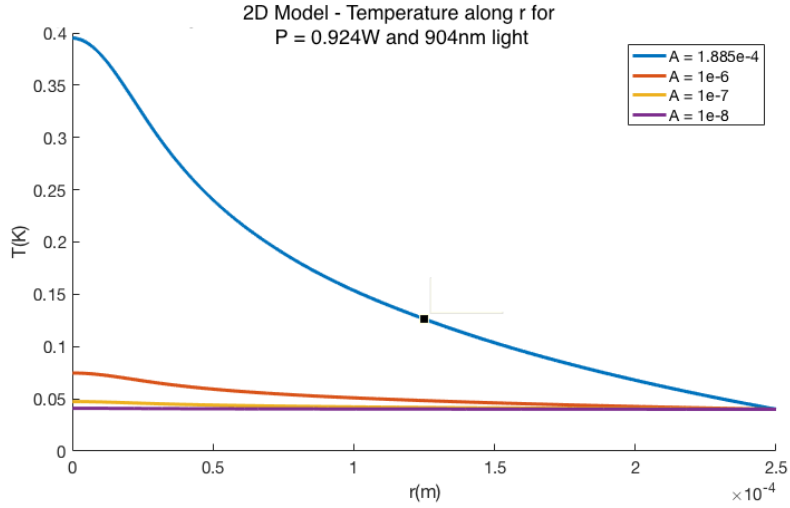
The **minimum optical absorption that corresponds to this temperature is  $\approx 10^{-4}$**  (Fig. 5.9), which is four orders of magnitude larger than what is expected from the preceding

Figure 5.8: A schematic of the setup used to measure Si PnC membrane ringdowns with varying base temperature and optical power. A network analyzer (NA) excites membrane modes that are detected via interferometry. The amplitude of the signal decays exponentially when the NA is disconnected, which allows to measure ringdowns,



sections, and even larger than what is usually assume in the community, i.e.,  $A_{\text{opt}} \leq 10^{-6}$  for high stress silicon nitride. It is possible that the optical absorption of silicon nitride has a very large wavelength dependence, but more likely the 904nm light in a cavity designed for 1064nm may have affected many aspects of the how the light was absorbed.

Figure 5.9: Temperature profile for different absorption values. Notice that to obtain the temperature predicted by the experimentally fitted  $T(P)$  relation, the absorption has to be at least four orders of magnitude larger than the necessary for other experiments, which is entirely unreasonable.

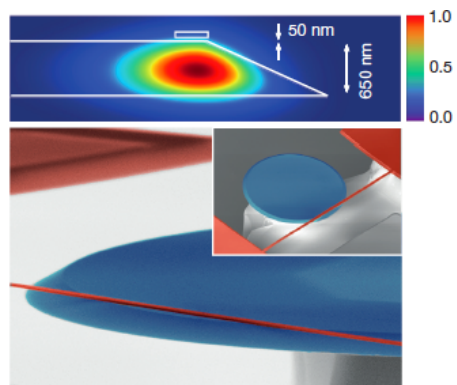


#### 5.4.4 850nm Tether Heating

The 1D heat equation 5.15 can be used to compare the heating of a membrane to that of a tether such as the one described on Wilson et al. [40], which is a whispering-gallery resonator whose trapped light evanescent field causes an adjacent tether to oscillate.

For the 1D simulation, we use the tether dimensions in table 5.5, and the substantial heating observed for  $T_{\text{base}} = 2.5\text{K}$  and  $P_{\text{in}} = 1\mu\text{W}$ . Wilson et al. observed "a dramatic rise in temperature" of the tether below 4K (Fig. 5.11), and according to a email conversation with one of the paper's authors, they "could observe the linear-in-power trend between 1 – 2 K, with injected powers of 0.1 – 4 $\mu\text{W}$ . At higher powers, < 2K, it proved difficult to avoid artifacts from optical and/or

Figure 5.10: Cavity optomechanics geometry of Wilson et al. [40]. The evanescent field of the light trapped in the whispering gallery couples with the adjacent tether (Image credit: Wilson et al. [40]).

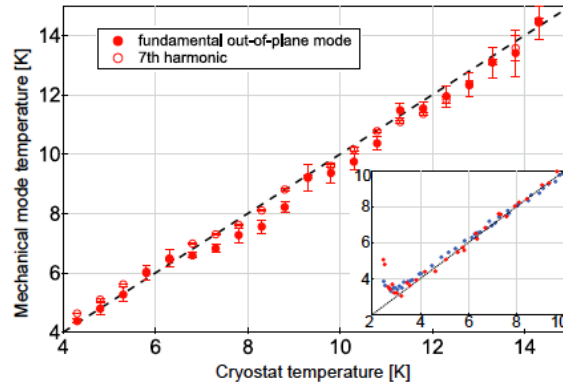


mechanical nonlinearities.

Table 5.5: Wilson et al. tether parameters [40].

|           |                          |
|-----------|--------------------------|
| Length/2  | $65/2 = 32.5\mu\text{m}$ |
| Width     | 400nm                    |
| Thickness | 70nm                     |

Figure 5.11: As the base temperature of the cryostat in which the system in Fig. 5.10 was located decrease below 4K, the tether heated substantially (inset).



Considering an injected power of 1W on the whispering gallery above, we need to figure out how much power is inside the cavity and which fraction of this power is circulating in the tether. The mean number of reflections of a photon in a cavity is  $N = \tau/t_{\text{trip}}$ ,  $\tau = 1/\Delta\omega_{\text{FWHM}} = 1/910 = 1.749 \times 10^{-10}\text{s}$ , and  $t_{\text{trip}} = \pi d/c = 4.13 \times 10^{-13}\text{s}$ . Therefore, for the whispering gallery cavity  $\bar{N} = 371$ .

Through correspondence the author told us that the fraction of power lost to the tether is around 1/2. Thus, if the injected power in the whispering gallery cavity is  $1\mu\text{W}$  and  $\bar{N} = 371$ , the power in the tether will be

$$P = 1\mu\text{W} \times \frac{371}{2} = 186\mu\text{W} \quad (5.22)$$

Considering a base temperature of  $T_{\text{base}} = 2.5\text{K}$  and guessing a heating of 1K, besides the thermal conductivity at  $T = 3\text{K}$  in table 5.2, the **absorptions that best agree are those above**  $A_{\text{opt}} =$

$10^{-6}$  (Fig. 5.12). Unfortunately, this lower bound also does not seem very reasonable. However, the values provided by the authors are very rough approximates, since they did not keep a detailed track of powers at low temperatures.

Figure 5.12: 1D model results for the maximum temperature of the tether in [40]. The minimum absorption for the heating observed is  $A_{\text{opt}} = 10^{-6}$ , which disagrees with the values of section .

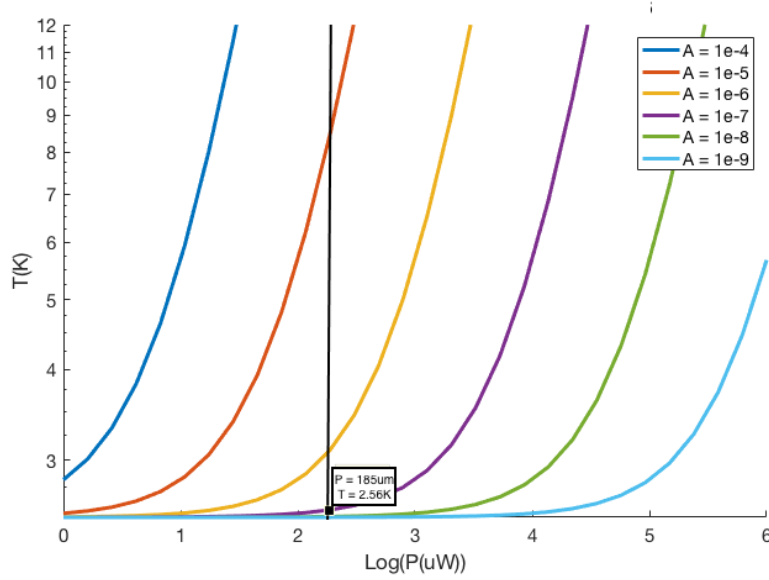


Table 5.6: Summary of the Calculated Optical Absorption Minima for Different Experimental Data Points.

| Data Point   | Thermal Conductivity                  | Optical Absorption                   |
|--|---------------------------------------|--------------------------------------|
| 1) $\lambda = 1064\text{nm}$ ,<br>$T_{\text{base}} = 40\text{mK}$ , $T = 140\text{mK}$   | $K(T) = (1.45 \times 10^{-2})T^{1.8}$ | $10^{-6} > A_{\text{opt}} > 10^{-8}$ |
| 2) $\lambda = 1064\text{nm}$ ,<br>$T_{\text{base}} = 4.6\text{K}$ , $T \sim 4.9\text{K}$ | $K(T) = (5.2 \times 10^{-3})T^{1.8}$  | $10^{-6} > A_{\text{opt}} > 10^{-9}$ |
| 3) $\lambda = 904\text{nm}$ ,<br>$T_{\text{base}} = 40\text{mK}$ , $T \sim 450\text{mK}$ | $K(T) = (1.45 \times 10^{-2})T^{1.8}$ | $A_{\text{opt}} > 10^{-4}$           |
| 4) $\lambda = 850\text{nm}$ ,<br>$T_{\text{base}} = 2.5\text{K}$ , $T \sim 3.5\text{K}$  | $K(T = 3\text{K}) = 0.13\text{W/mK}$  | $A_{\text{opt}} > 10^{-6}$           |

## Chapter 6

### Conclusion

In summary, this thesis has presented models and calculations that characterize the losses and limitations of high-stress silicon nitride resonators, especially in the context of cavity optomechanics, and uses this understanding to design improved resonators. We started with a discussion of cavity optomechanics and how the strong coupling between optical and mechanical modes can be used to cooldown a macroscopic object to its ground state and access its quantum behavior. In particular,  $\text{Si}_3\text{N}_4$  membranes have shown incredible performance when placed inside optical cavities. Nonetheless, both external and internal losses limit how well they decouple from external, thermal “noise,” which leads to an intense interest in  $\text{Si}_3\text{N}_4$  resonator designs that will greatly decrease these losses.

Patterning the substrate surrounding a resonator with a high-mass, low-mass phononic crystal (PnC) allows for a very large reduction of external losses, which happen when membrane modes extend to the substrate, inducing its motion and therefore taking energy away from the resonator. By having a phononic crystal designed around the membrane, one can place some membrane modes inside the bandgap of the crystal, which guarantees the membrane modes will be incapable of exciting the substrate. This approach has been implemented successfully by the Regal group, and the Silicon PnC structures have very high quality factors of  $\sim 10^7$ , about an order of magnitude higher than for pure membranes.

Another approach addresses mostly the bending at the edges, the biggest factor in the internal losses for a  $\text{Si}_3\text{N}_4$  membrane. By producing a tethered membrane also known as a trampoline, the

bending at the clamping edges is greatly reduced (together with the connection with the substrate), improving  $Q_s$  one to two orders of magnitude.

A third design results from implementing a PnC directly into the  $\text{Si}_3\text{N}_4$ , allowing for a small central defect area to play the role of “membrane.” Not only is the external loss extremely small if enough unit cells are included, but also the bending at the PnC-defect edge is greatly reduced, which have been shown to boost the quality factors of such structures to  $10^8$ .

Quite naturally, we expect then that a  $\text{Si}_3\text{N}_4$  PnC with a trampoline defect may have even greater  $Q_s$ , perhaps  $\sim 10^9$ . Moreover, a trampoline’s reduced mass improves the force sensitivity of these hybrid resonators, which is also great interest. In particular, in this thesis two hybrid trampoline-PnC designs have been modeled and characterized, both adapted to the Regal group’s current cavity optomechanics and force sensing demands, which requires smaller structures of potentially higher frequencies and smaller masses. The very immediate future direction in this front is to measure the  $Q_s$ , both at room and at cryogenic temperatures, for fabricated hybrid structures. Moreover, we also intend to use an analytical model recently developed by the Sankey group in Canada to understand better how the unit cell geometry affects the bandgap size, position, and the necessary number of unit cells required for good mode defect mode isolation. This would allow us to create even better, smaller hybrid PnCs.

Finally, calculations of the lower bounds for the optical absorption of  $\text{Si}_3\text{N}_4$  were discussed. Past experiments where membranes were cooled down to their ground state and the brownian motion of the resonators due to the intracavity optical field indicated that the optical absorption of  $\text{Si}_3\text{N}_4$  had to be very small. Fitting the data using 2D and 1D heat equations with thermal conductivity values from the literature revealed that very low optical absorption is indeed a likely property. Nonetheless, a few discrepancies have arisen in these analysis. Therefore, we plan to perform further measurements of the temperature as a function of input power in the near future.

## Bibliography

- [1] Abbott, B. P. et al. "Observation of Gravitational Waves from a Binary Black Hole Merger." *Phys. Rev. Lett.* **116**, 061102 (2016).
- [2] Aspelmeyer, M., Meystre, P. & Schwab, K. "Quantum optomechanics." *Physics Today* **65**, 29 - 35 (2012).
- [3] Meystre, P. "A short walk through quantum optomechanics." *Annalen der Physik* **525**, 215 - 233 (2013).
- [4] Purdy, T. P., Peterson, R. W., Yu, P.-L. & Regal, C. A. "Cavity optomechanics with Si<sub>3</sub>N<sub>4</sub> membranes at cryogenic temperatures." *New J. Phys.* **14**, 115021 (2012).
- [5] Andrews, R. W. et al. "Bidirectional and efficient conversion between microwave and optical light." *Nature Physics* **10**, 321 - 326 (2014).
- [6] Peterson, R. W. et al. "Laser Cooling of a Micromechanical Membrane to the Quantum Back-action Limit." *Physical Review Letters* **116**, (2016).
- [7] Schwab, K. C. & Roukes, M. L. "Putting mechanics into quantum mechanics." *Physics Today* **58**, 36 - 42 (2005).
- [8] Jayich, A. M. et al. "Dispersive optomechanics: a membrane inside a cavity." *New Journal of Physics* **10**, 095008 (2008).
- [9] Sidles, J. A. & Rugar, D. "Signal-to-noise ratios in inductive and mechanical detection of magnetic resonance." *Physical review letters* **70**, 3506 (1993).
- [10] Wilson-Rae, I. "Intrinsic dissipation in nanomechanical resonators due to phonon tunneling." *Physical Review* **B 77**, (2008).
- [11] Cole, G. D., Wilson-Rae, I., Werbach, K., Vanner, M. R. & Aspelmeyer, M. "Phonon-tunnelling dissipation in mechanical resonators." *Nature Communications* **2**, 231 (2011).
- [12] Unterreithmeier, Q. P., Faust, T. & Kotthaus, J. P. "Damping of Nanomechanical Resonators." *Physical Review Letters* **105**, (2010).
- [13] Schmid, S., Jensen, K. D., Nielsen, K. H. & Boisen, A. "Damping mechanisms in high- Q micro and nanomechanical string resonators." *Physical Review* **B 84**, (2011).

- [14] Yu, P.-L., Purdy, T. P. & Regal, C. A. “Control of Material Damping in High- Q Membrane Microresonators.” *Physical Review Letters* **108**, (2012).
- [15] Yu, P.-L. et al. “A phononic bandgap shield for high-Q membrane microresonators.” *Applied Physics Letters* **104**, 023510 (2014).
- [16] Norte, R. A., Moura, J. P. & Grblacher, S. “Mechanical Resonators for Quantum Optomechanics Experiments at Room Temperature.” *Physical Review Letters* **116**, (2016).
- [17] Reinhardt, C., Mller, T., Bourassa, A. & Sankey, J. C. “Ultralow-Noise SiN Trampoline Resonators for Sensing and Optomechanics.” *Physical Review X* **6**, (2016).
- [18] Tsaturyan, Y., Barg, A., Polzik, E. S. & Schliesser, A. “Ultra-coherent Nanomechanical Resonators Via Soft Clamping and Dissipation Dilution.” arXiv preprint arXiv:1608.00937 (2016).
- [19] Scozzaro, N. et al. “Magnetic resonance force detection using a membrane resonator.” arXiv preprint arXiv:1603.03953 (2016).
- [20] Butler, M. C., Norton, V. A. & Weitekamp, D. P. “Nanoscale Torsional Resonator for Polarization and Spectroscopy of Nuclear Spins.” *Physical Review Letters* [?], (2010).
- [21] Marquardt, F. & Girvin, S. “Optomechanics.” *Physics* **2**, (2009).
- [22] Aspelmeyer, M., Kippenberg, T. J. & Marquardt, F. ”Cavity optomechanics.” *Reviews of Modern Physics* **86**, 1391-1452 (2014).
- [23] Thompson, J. D. et al. “Strong dispersive coupling of a high-finesse cavity to a micromechanical membrane.” *Nature* **452**, 72 - 75 (2008).
- [24] Corbitt, T. et al. “An All-Optical Trap for a Gram-Scale Mirror.” *Physical Review Letters* **98**, (2007).
- [25] Wilson, D. J., Regal, C. A., Papp, S. B. & Kimble, H. J. “Cavity Optomechanics with Stoichiometric SiN Films.” *Phys. Rev. Lett.* **103**, 207204 (2009).
- [26] Purdy, T. P., Peterson, R. W. & Regal, C. A. “Observation of Radiation Pressure Shot Noise on a Macroscopic Object.” *Science* **339**, 798 - 801 (2013).
- [27] Purdy, T. P., Yu, P.-L., Peterson, R. W., Kampel, N. S. & Regal, C. A. “Strong Optomechanical Squeezing of Light.” *Physical Review X* **3**, (2013).
- [28] Degen, C. L., Poggio, M., Mamin, H. J. & Rugar, D. “Nuclear Spin Relaxation Induced by a Mechanical Resonator.” *Physical Review Letters* **100**, (2008).
- [29] Bruland, K. J., Dougherty, W. M., Garbini, J. L., Sidles, J. A. & Chao, S. H. “Force-detected magnetic resonance in a field gradient of 250 000 Tesla per meter.” *Applied Physics Letters* **73**, 3159 (1998).
- [30] Rugar, D., Budakian, R., Mamin, H. J. & Chui, B. W. “Single spin detection by magnetic resonance force microscopy.” *Nature* **430**, 329 - 332 (2004).
- [31] Rawat, U., Pasula, V. V., Nair, D. R. & DasGupta, A. “Efficient Anchor Design for Quality Factor Enhancement in a Silicon Nitride-on-Silicon Lateral Bulk Mode Resonator.” Paper presented at COMSOL Conference Bangalore (2015).

- [32] Simon, S. H. *The Oxford Solid State Basics*. Oxford University Press: New York, NY. (2016).
- [33] Bindel, D. S. & Govindjee, S. “Elastic PMLs for resonator anchor loss simulation.” *International Journal for Numerical Methods in Engineering* **64**, 789 - 818 (2005).
- [34] Wang, J., Butler, J. E., Feygelson, T. & Nguyen, C.-C. “1.51-GHz nanocrystalline diamond micromechanical disk resonator with material-mismatched isolating support.” in *Micro Electro Mechanical Systems, 2004. 17th IEEE International Conference on.(MEMS)* 641 - 644 (IEEE, 2004).
- [35] Schwab, K., Henriksen, E. A., Worlock, J. M. & Roukes, M. L. “Measurement of the quantum of thermal conductance.” *Nature* **404**, 974 - 977 (2000).
- [36] Pohl, R. O., Liu, X. & Thompson, E. “Low-temperature thermal conductivity and acoustic attenuation in amorphous solids.” *Reviews of Modern Physics* **74**, 991 (2002).
- [37] Leivo, M. M. & Pekola, J. P. “Thermal characteristics of silicon nitride membranes at sub-Kelvin temperatures.” *Applied Physics Letters* **72**, 1305 (1998).
- [38] Ftouni, H. et al. “Specific heat measurement of thin suspended SiN membrane from 8 K to 300 K using the  $3\omega$ -Viklein method.” *Review of Scientific Instruments* **84**, 094902 (2013).
- [39] Zink, B. L. & Hellman, F. “Specific heat and thermal conductivity of low-stress amorphous SiN membranes.” *Solid State Communications* **129**, 199 - 204 (2004).
- [40] Wilson, D. J. et al. “Measurement-based control of a mechanical oscillator at its thermal decoherence rate.” *Nature* **524**, 325 - 329 (2015).